This is a repository copy of *Gradual caldera collapse at Bárdarbunga volcano, Iceland, regulated by lateral magma outflow*.

White Rose Research Online URL for this paper:
http://eprints.whiterose.ac.uk/103058/

Version: Accepted Version

Gradual caldera collapse at Bárdarbunga volcano, Iceland, regulated by lateral magma outflow

Magnús T. Gudmundsson[1], Kristín Jónsdóttir[2], Andrew Hooper[3], Eoghan P. Holohan[4,5], Saemundur A. Halldórsson[1], Benedikt G. Ófeigsson[2], Simone Cesca[4], Kristín S. Vogfjörd[2], Freysteinn Sigmundsson[1], Thórdís Högnadóttir[1], Páll Einarsson[1], Olgeir Sigmarsson[1,6], Alexander H. Jarosch[1], Kristján Jónasson[7], Eyjólfur Magnússon[1], Sigrún Hreinsdóttir[8], Marco Bagnardi[3], Michelle M. Parks[1], Vala Hjörleifsdóttir[9], Finnur Pálsson[1], Thomas R. Walter[4], Martin P.J. Schöpfer[10], Sebastian Heimann[4], Hannah I. Reynolds[1], Stéphanie Dumont[1], Eniko Bali[1], Gudmundur H. Gudfinnsson[1], Torsten Dahm[4], Matthew Roberts[2], Martin Hensch[2], Joaquín, M.C. Belart[1], Karsten Spaans[3], Sigurdur Jakobsson[1], Gunnar B. Gudmundsson[2], Hildur M. Fridriksdóttir[1,2], Vincent Drouin[1], Tobias Dürig[1], Gudfinna Adalgeirsdóttir[1], Morten S. Riishuus[1], Gro B.M. Pedersen[1], Tayo van Boeckel[1] , Björn Oddsson[11], Melissa A. Pfeffer[2], Sara Barsotti[2], Baldur Bergsson[2], Amy Donovan[12], Mike R. Burton[13], Alessandro Aiuppa[14]

1: Nordvulk, Institute of Earth Sciences, University of Iceland, Sturlugata 7, 101 Reykjavík

2: Icelandic Meteorological Office, IS-150 Reykjavík, Iceland

3: Centre for the Observation and Modelling of Earthquakes, Volcanoes and Tectonics (COMET), School of Earth and Environment, University of Leeds, Leeds LS2 9JT, UK

4: GFZ German Research Centre for Geosciences, Telegrafenberg, 14473 Potsdam, Germany

5: UCD School of Earth Sciences, University College Dublin, Ireland

23

6: *Laboratoire Magmas et Volcans, CNRS-Université Blaise Pascal-IRD, 63038 Clermont-Ferrand, France*

7: *Faculty of Industrial and Mechanical Engineering and Computer Science, University of Iceland, Hjarðarhagi 2-6, 107 Reykjavík, Iceland*

8: *GNS Science, PO Box 30368, Lower Hutt 5040, New Zealand*

9: *Departamento de Sismología, Instituto de Geofísica, Universidad Nacional Autónoma de Mexico, 04510 Ciudad de México, Mexico*

10: *Department for Geodynamics and Sedimentology, University of Vienna, Althanstrasse 14, A-1090 Vienna, Austria.*

11: *National Commissioner of the Icelandic Police, Department of Civil Protection and Emergency Management, Skúlagata 21, 101 Reykjavík, Iceland*

12: *King's College London, King's Building, Strand Campus, London WC2R 2LS, England, United Kingdom*

13: *University of Manchester, Williamson Building, Oxford Road, Manchester, M13 9PL, UK*

14: *University of Palermo – Piazza Marina, 61 90133, Palermo, Italy*

40 **Abstract**

41 Large volcanic eruptions on Earth commonly occur with collapse of the roof of a crustal magma

42 reservoir, forming a caldera. Only a few such collapses occur per century and lack of detailed

43 observations has obscured insight on mechanical interplay between collapse and eruption. We use

44 multi-parameter geophysical and geochemical data to show that the 110 km^2 and 65 m deep

45 collapse of Bárdarbunga caldera in 2014-15 initiated through withdrawal of magma, and lateral

46 migration through a 47 km long dyke, from a 12 km deep reservoir. Interaction between the

47 pressure exerted by the subsiding reservoir roof and the physical properties of the subsurface flow

48 path explain the gradual, near exponential decline of both collapse rate and the intensity of the 181-

49 day long eruption.

50 ⎯⎯⎯⎯⎯⎯⎯⎯⎯⎯

51

52 Calderas are 1 - 100 km diameter depressions found in volcanic regions of Earth and other planets.

53 They mainly form by collapse of overburden into a subterranean magma reservoir during large

54 volcanic eruptions, including the largest known super-eruptions (*1-8*). From 1900 AD to 2014, only

55 six cases have been documented and with varying degrees of detail. The collapses of Katmai in

56 1912 and Pinatubo in 1991 occurred during explosive silicic (andesite-rhyolite) eruptions, the

57 largest of the 20th century. The collapses of Fernandina in 1968, Tolbachik in 1975-76, Miyakejima

58 in 2000 and Piton de la Fournaise in 2007 were associated with mainly effusive mafic (basalt –

59 basaltic andesite) intrusive activity and eruptions (*2, 9-12*).

60 The consensus from field and modelling studies is that caldera collapse progresses from initial

61 surface downsag to fault-controlled subsidence (*1, 8, 13, 14*). The limited number of modern

62 examples and the scarcity of geophysical data leaves open the question of whether collapse occurs

63 suddenly or gradually during the course of an eruption. The issue of whether collapse drives magma

64 movement and eruption or eruption drives collapse also remains unresolved. Previous geological,

geophysical, and modeling studies have produced a diverse and inconsistent set of answers to such

questions (*2*, *4*, *15*, *16*). The caldera collapse at Bárdarbunga in central Iceland from August 2014 to

February 2015 offers a unique opportunity to address them directly.
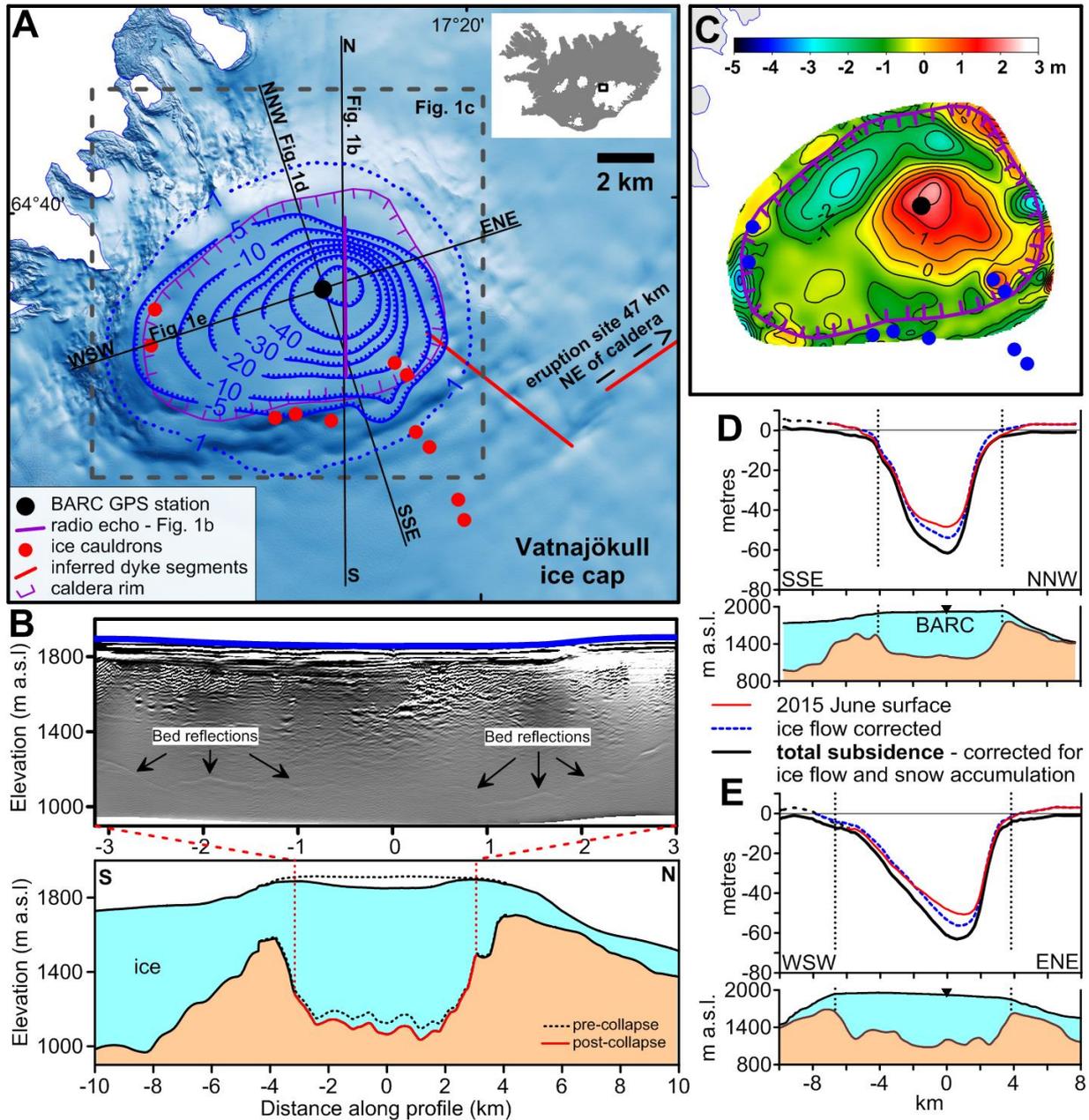
Figure 1. Bárdarbunga and geometry of collapse. A) Map showing the total caldera subsidence

(in meters) at the end of collapse in February 2015þ Minor sustained geothermal activity, monitored

from aircraft, increased during the collapse with pre-existing ice cauldrons deepening by up to 50 m

and new ones forming at the southern margin and to the southeast of the caldera (*24*). (B) Radio-

echo sounding profile from 3 February, 2015, and a cross-section of the caldera with the collapse.

The Bárdarbunga volcano and the Holuhraun eruption of 2014-15

Bárdarbunga volcano (Fig. 1) and its related fissure swarms form a 150 km long volcanic system on the boundary between the North-American and Eurasian tectonic plates. The volcano resides beneath the Vatnajökull ice cap and has a broadly elliptic 13 by 8 km wide and 500-700 m deep caldera with a long axis trending ENE. About 700-800 m of ice fills the caldera (*17*, *18*). Over 20 eruptions have occurred on the fissure swarms outside the caldera in the last 12 centuries, including three that produced 1-4 km^3 of magma, but no eruptions are known within the caldera in this period. (*19*).

At 4 UTC on 16 August 2014, the onset of intense seismicity beneath the caldera marked the beginning of a major rifting event (*20*). The seismic activity was mostly located in the SE-corner of the caldera in the first few hours, but it soon began to propagate out of the caldera towards the SE (Fig. 2). After propagating to about 7 km from the caldera rim, fifteen hours after the onset of seismicity (~19 UTC), the moving earthquake cluster took a 90° turn and started migrating towards the NE. In the two weeks that followed, surface deformation and migration of seismicity indicated that a magmatic dike propagated laterally northeastward for 47 km in the uppermost 6-10 km of the Earth's crust (*20*, *21*). On 31 August, a major effusive eruption began above the far end of the dike; this lasted six months and produced 1.5±0.2 km^3 of lava (~1.4±0.2 km^3 of bubble-free magma) (*22*), making it the largest in Iceland (or Europe) since the 1783-84 Laki eruption. Combined with

98   the 0.5±0.1 km^3 dyke (*20*), the total volume of identified intruded and erupted magma was 1.9±0.3

99   km^3.

The Onset of Collapse

101   After the initial seismic activity in the caldera receded late on 16 August, seismicity was relatively

102   minor there until 20 August. At the same time our GPS time-series from stations close to the

103   caldera, suggest that deflation of the magma reservoir started on 16 August (*20*).   On 20 August,

104   caldera seismicity increased progressively with a series of earthquakes of magnitude M4-M5.8

105   occurring in the following days (Fig. 2). The first two events occurred on the southern caldera rim

106   (M4.7 on 20 August and M5.1 on 21 August). Following these earthquakes, three similar magnitude

107   events occurred on the northern rim on 23 August, followed by four events on the southern rim on

108   24-25 August. On 26 August activity shifted again to the northern rim with a M5.8 earthquake, the

109   largest in the whole series. These data indicate that significant movement on ring faults started on

110   the south side with the 20-21 August earthquakes, then began on the north side on 23 August, and

111   by 24 August the ring faults on both sides where slipping, a process that did not terminate until at

112   the end of February. Onset of collapse therefore likely occurred on 20 August with the ring fault

113   fully activated on 24 August. If we compare the evolution of the dike together with the seismic

114   moment release of the caldera collapse earthquakes, we can clearly see that the dike migration leads

115   the moment release curve (Fig. 2A).   We therefore conclude that onset of collapse resulted from a

116   pressure drop in the reservoir as magma was laterally withdrawn into the propagating dike, with the

117   latter possibly primarily driven by regional tectonic tensional stresses (*20*).

118   The volume of the expanding dike on 20 August had reached approximately 0.25 km^3, increasing to

119   0.35 km^3 on 24 August (*20*) with the source of this magma being the reservoir beneath the caldera.

120   The relatively minor caldera seismicity on 17-19 August indicates the material overlying the

121   magma reservoir deformed mostly elastically until it reached a critical failure point of caldera

122   collapse on 20-24 August. If we assume that the entire volume of eruptible magma within the

123   reservoir was 1.9±0.2 km³, then the critical volume fraction required to reach the failure point and

124   trigger the collapse (*23*) was 0.12-0.21.

125
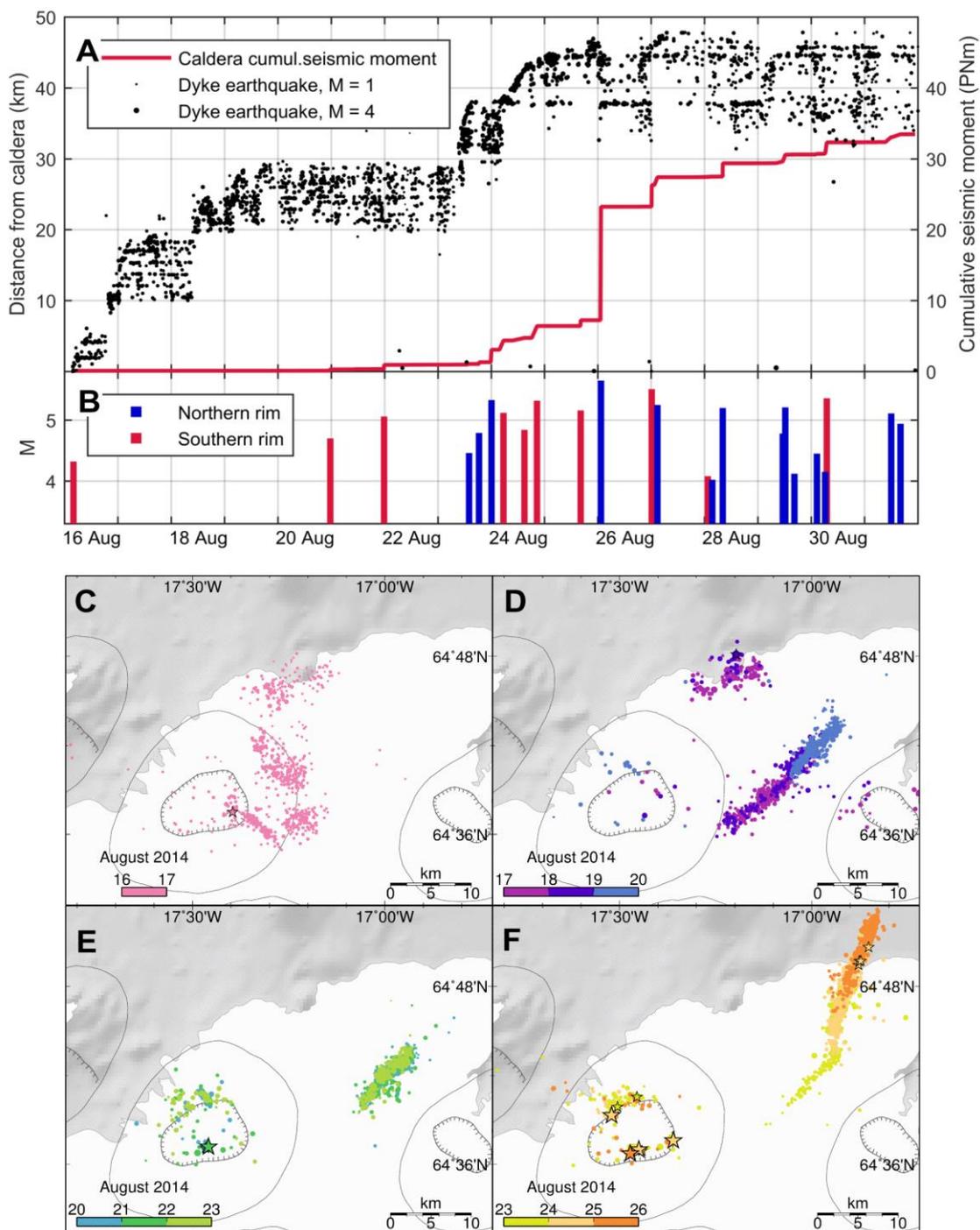
126

127   **Figure 2. Onset of caldera collapse**. A) Cumulative seismic moment release from caldera

128   earthquakes plotted together with distribution of seismicity along the dike length, using high quality

relative locations of earthquakes (*20*), for the time period when the dike progressed away from the caldera. B) Significant caldera earthquakes with magnitudes above M4 plotted as impulses, where the height represents magnitude and color represents location on southern or northern rim. C) Map of NW Vatnajökull showing earthquake epicenters on 16 August, D) 17-19 August, E) 20-22 August and F) 23-15 August.

Ice Flow, Subsidence Magnitude and Volume

As we recorded the caldera subsidence mainly on the ice (Fig. 1, Fig. S1), we made corrections and additional measurements to derive the underlying bedrock displacement. Our main data on ice surface changes and ice movements are repeated C-band radar altimeter surveys from aircraft, maps made from optical satellite images and the continuously recording GPS station BARC we set up in the center of the caldera on 13 September. The observed velocities and displacements of the ice surface are displayed on Figs. 3A and 3B. We use these observations to constrain three-dimensional Full-Stokes finite element modelling of ice-flow in response to the collapse (*24*). The results show concentric flow, towards the point of maximum collapse within the caldera, with maximum ice thickening at the center of ~3 m by February 2015 (Fig. 1C, Fig. S2). The maximum ice surface lowering of 62±2 m, determined by aerial altimeter surveys, gives a maximum bedrock subsidence of 65±3 m. Our data and models show that apart from the concentric flow towards the deepest part of the subsidence (about 1 km east of BARC) horizontal flow was not much affected (Fig. 3A). We therefore conclude that suggestions of a large increase in ice flow out of the caldera during these events (*25*) cannot be fitted with our data.

Bedrock subsidence exceeding 1 m occurred within an area of 110 km^2 that extended beyond the pre-existing caldera (Fig. 1, Fig. S1). After termination of collapse the total subsidence at the pre-existing caldera rims amounted to 3 to 11 meters (Fig. 1D and 1E). Using subglacial radio-echo soundings we observed a down-sagged bedrock surface without any clear signs of fault offset (Fig 1B) or indications of water bodies at the ice bedrock interface. The limited resolution resulting

154   from the 600-800 m ice thickness means that we cannot on the basis of the radio-echo results

155   exclude the possibility of steep fault escarpments. However, substantial vertical fault movement at

156   the base of the glacier would result in high strain rates within the basal ice which would instantly

157   fracture the ice fabric and propagate upward. During drainage of subglacial lakes in Iceland, large

158   surface fractures induced by basal motion have been observed repeatedly (*26*) and can serve here as

159   an analog for the possible surface manifestations of vertical basal motion. The absence of such

160   surface ice fractures at Bárdabunga indicates that no substantial fault escarpment formed at the

161   bottom. The calculated collapse volume is 1.8 ± 0.2 km^3, not significantly different from the

162   combined volume of erupted and intruded magma (Fig. 3B).

163
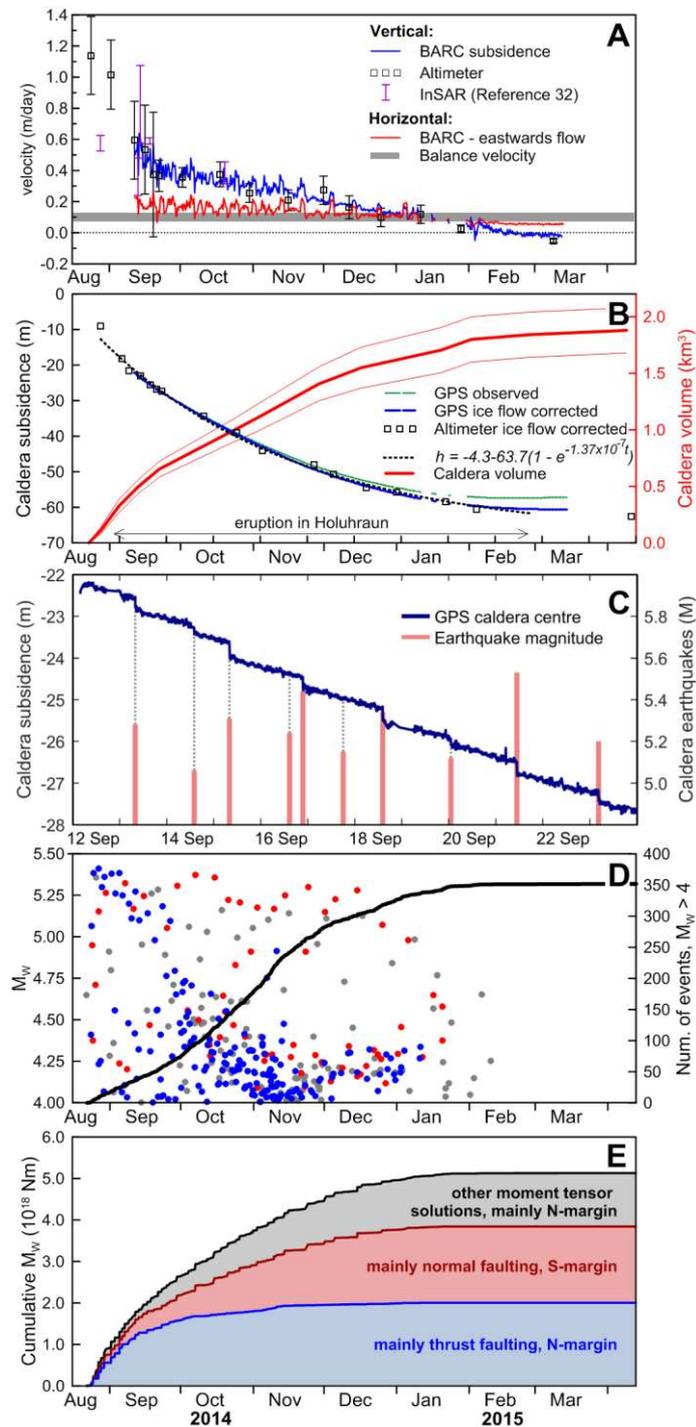
Figure 3. Time series of collapse. A) Vertical and horizontal velocities measured at the BARC

GPS station in the center of the caldera (Fig. 1A), including the rate of vertical rate of ice surface

subsidence found from altimeter aircraft data and optical satellite photogrammetry. The balance

velocity is obtained by estimating the rate of displacement required to transport the net

accumulation of the area draining ice towards east in the western part of the caldera. InSAR

derived vertical velocities are based on (*32*). B) Subsidence at the center of the caldera and

Magma source depth

Lava chemistry, surface gas composition and geodetic modelling indicate drainage of a magma

reservoir at a depth of ~12 km. The erupted lava is typical olivine tholeiite with a relatively uniform

chemical composition, consistent with efficient homogenization of melts before eruption. Several

independent geobarometers (Fig. 4) yield an equilibrium pressure of 350-550 MPa, indicating that

melt resided at depths of 11-16 km before the eruption. We obtained a similar result (14±3 km)

from analysis of subaerial gas measurements (Fig. 4). This depth concurs with our regional

geodetic observations, which are dominated by a deflating source at 8-12 km depth beneath

Bárdarbunga, after the cessation of dike-related deformation in mid-September (Figs. S3 and S4).
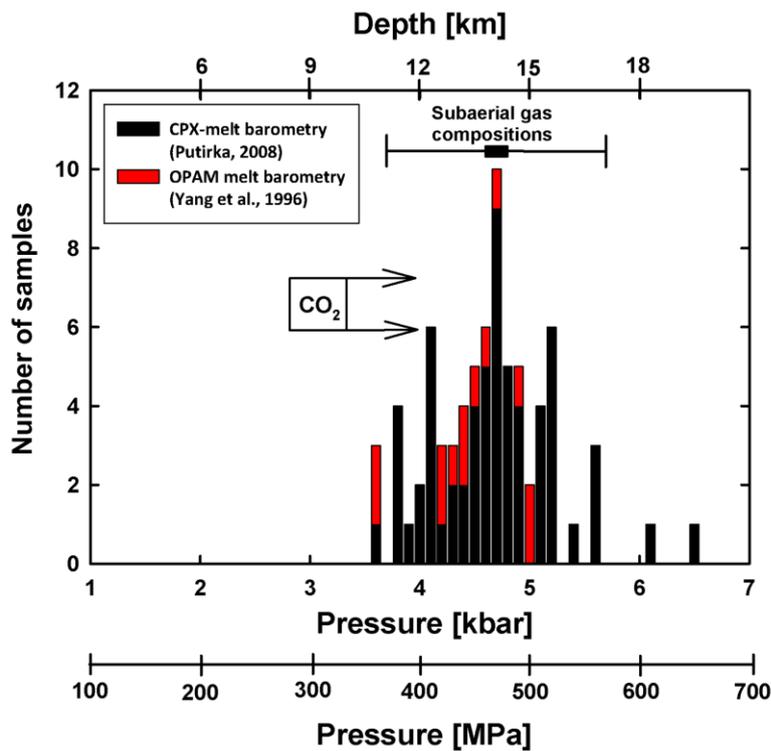
Figure 4. Magma source depth from geobarometric and subaerial gas analysis. The CO2-box indicates the minimum pressure obtained (400 kbar) from density barometry of plagioclase hosted CO2-bearing fluid inclusions. The results from the analysis of subaerial gas compositions are based on FTIR and Multi-GAS measurements (*24*).

Seismicity and subsurface structure

We used seismic data and Distinct Element Method (DEM) numerical modelling (*24*), to characterize the deeper collapse structure as the reactivation of a steeply-inclined ring fault (Fig. 5). We mostly observed seismicity at depths of 0-9 km beneath the northern and southern caldera rims (Fig. 5B), with earthquakes being more numerous on the northern rim. This spatial pattern of seismicity is consistent with fracturing above a deflating magma reservoir that was elliptical in plan-view (*27*). In cross-section, the hypocenters indicate a steeply (~80°) outwards-dipping fault in the northern cluster, while the southern cluster they indicate a vertical or near-vertical fault dip. A series of DEM forward simulations of a magma chamber and ring fault system, as constrained by

12

204   the hypocenter distribution and by the geobarometry data, tested the above structural interpretation

205   against the observed NNW-SSE subsidence profile. The models indicate that a pre-existing and

206   relatively low friction (coefficient of 0.1-0.2) ring-fault system controlled the subsidence at depth

207   (Fig. 5C, D). Our best fitting models had preexisting faults dipping out at 80-85° from the caldera

208   center on the north side and at 85-90° toward the caldera center on the south side. The modeled pre-

209   existing faults lay at 1-2 km below the surface on the north side and 3-4 km on the south side.

210   Modeling of a more complex fault geometry or the inclusion of greater material heterogeneity may

211   further improve the data fit, but presently lacks robust geophysical constraints. The arrangement of

212   an outward dipping fault on one side of a caldera and an inward-dipping fault on the other is typical

213   of 'asymmetric' or 'trapdoor-like' collapses produced in past analog and numerical modeling

214   studies (*8*, *28*, *29*). It also occurs at Glencoe (*29*) and Tendurek (*30*) volcanoes . Finally, our finding

215   is consistent with past seismological results that defined a very similar ring-fault geometry during

216   the last period of activity at Bardarbunga in 1996 (*31*).

217   Through regional moment tensor (MT) inversion, we infer that the source mechanisms of 77 M>5

218   events (Fig. S5) confined to two clusters beneath the northern and southern rim regions show

219   contributions of both shear and non-shear components. The shear components indicate possible

220   ruptures of segments on the ring fault. Shear failure on inward dipping ring faults, or the sudden

221   injection of magma in horizontal fissures forming sills have been proposed (*32*) to explain the shear

222   components of the observed earthquakes at Bárdarbunga. We, however, narrowed down on

223   plausible solutions by using the micro-earthquakes (Fig. 5A). The moment tensor solutions are well

224   constrained, but the inferred dip of the shear plane we obtain is uncertain since the non-shear

225   component, in this case a negative, sub-vertical compensated linear vector dipole (vCLVD), is

226   dominant. As a result, the shear orientation obtained depends very much on the decomposition

227   approach.

228   By using the constraint of the steeply outward dipping ring fault on the northern cluster we derive a

229   MT solution that is a combination of a negative vCLVD and steep E-W striking reverse faulting

230   (Fig. 3D, 3E and Fig. S5). In contrast, standard decomposition of the northern cluster MTs provides

231   normal faulting along steep N-S striking planes, a result that is inconsistent with the observed main

232   fault orientation. The southern cluster MTs are consistent with being composed of families (*33*) of

233   steep normal faulting earthquakes.

234   The large, negative vCLVD indicates a combination of downward contraction and horizontal

235   expansion, as has been observed in mines as well as in volcanic calderas during collapses (e.g. *31*,

236   *34*). This could imply failure of support structures directly above or even within the magmatic

237   reservoir, or the sudden response of the reservoir fluid to vertical compression.

238   Temporal development of subsidence and related seismicity

239   Subsidence occurred gradually during the eruption (Fig. 3B). From an initial rate in the caldera

240   center of ~1 m/day during the first 20 days (Fig. 3B), subsidence declined in a near exponential

241   manner with time (24). Subsidence terminated when the eruption ended in February 2015. We can

242   associate some of the M>5 caldera earthquakes, during the first couple of months of activity, with

243   drops of 10-40 cm, but subsidence was otherwise continuous (Fig. 3C). The gradual decline in the

244   rates of subsidence and caldera volume growth is mirrored by a decline in the cumulative seismic

245   moment, the latter reflecting a decrease in the number of larger earthquakes with time (Fig. 3D, 3E).

246   Nonetheless, in terms of the cumulative seismic moment of 5.07×10^{18} Nm for the M>4.0 events,

247   this collapse is the second largest recorded, after that of Katmai (1912) (*35*). The geodetic moment

248   depends on the shear modulus, the fault area and the amount of slip assumed. The shear modulus

249   could be very low in regions of intense faulting such as on a caldera ring fault. The possible range

250   of the geodetic moment is found by considering a ring fault reaching from the surface to 12 km

251   depth, 60 m of slip and a shear modulus over a wide range, 2-20 GPa. This results in a moment of

252   4×10^{19} - 4×10^{20} Nm, or 10-100 times the cumulative seismic moment of the earthquakes.   This

253   difference is consistent with the modeling of surface deformation observed during one of the events

254   (Fig S7).

255
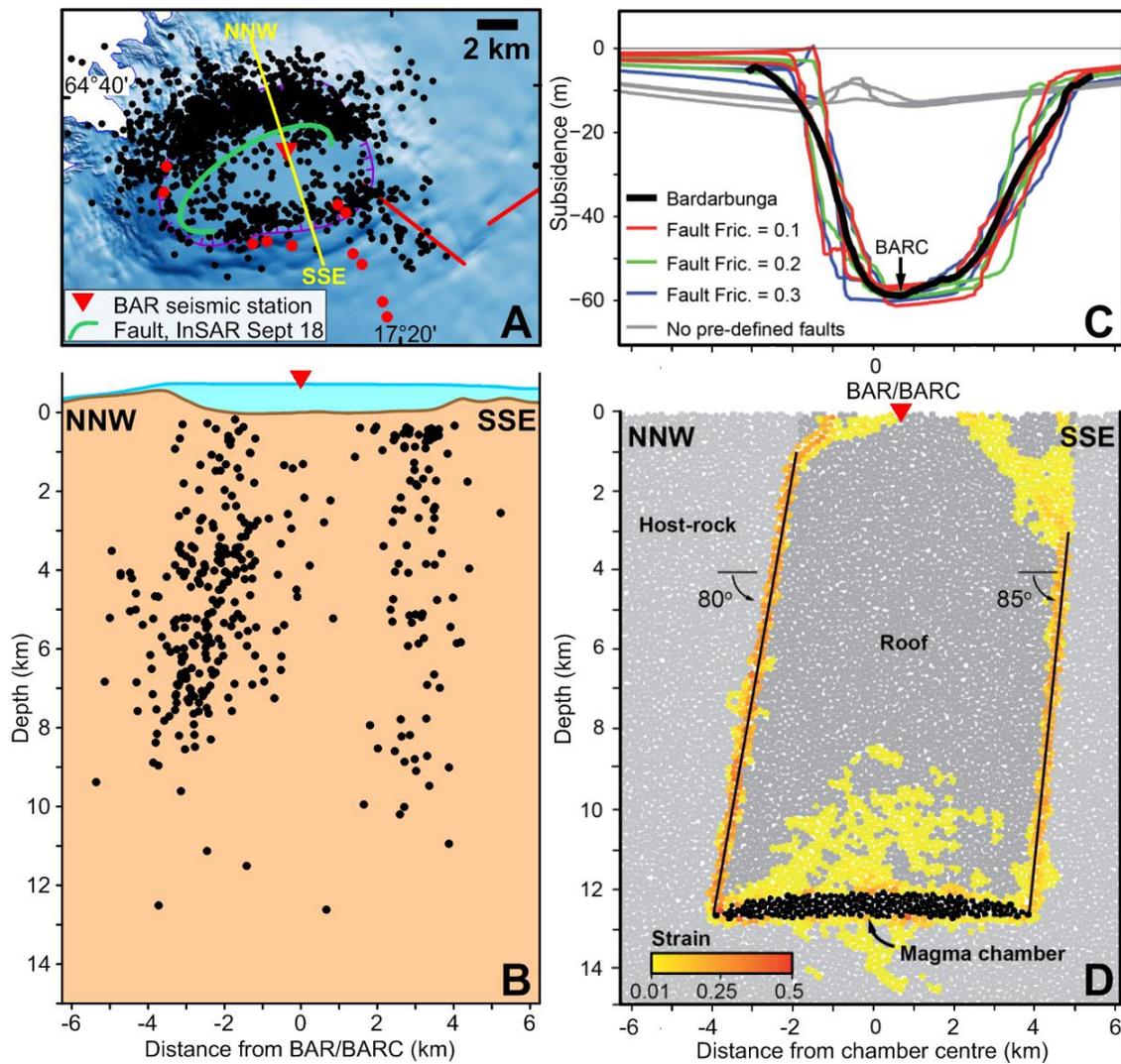
Figure 5: Fault geometry and collapse modelling: A) Earthquakes 1 August – 17 October 2014,

B) seismicity along a 2-4 km wide strip on the NNW-SSE cross section, depth relative to bedrock

caldera floor. C-D) Two-dimensional DEM modeling of the collapse, constrained by subsidence

geometry, earthquake locations in (B), and the geobarometry (Fig. 4). The geometry illustrated in

(D) obtained the best agreement with the observations. The color scale shows the maximum finite

shear strain. Surface displacement profiles for different pre-existing fault frictions are provided in

(C). Three model realizations are shown for each friction value.

Caldera-flowpath interaction and piston collapse modeling

We see a short-term (multi-hourly) mechanical coupling of the collapsing caldera and the distal dike (south of eruption site) in the timing of earthquakes in the dike and at the caldera (Fig. 6A). Within a six-hour window before and after large caldera earthquakes the frequency of dike earthquakes was increased relative to background rate (24). We observed this pattern in the data after the beginning of October 2014, when the dyke had stopped propagating and a quasi-steady magma flow path had developed, until February 2015 when seismic activity stopped. For the three hours after caldera earthquakes with magnitude $M > 4.6$, as well as for the three hours before caldera earthquakes with $M > 4.0$, the increase in seismicity was significant (*24*) ($p = 0.05$; Fig. 6, Fig. S8).

At Bárdarbunga communication therefore existed between caldera subsidence events and pressure changes in a conduit up to 47 km away. Spatiotemporal patterns of tilt at Kilauea Volcano, Hawaii, show a similar phenomenon that can be explained by the propagation of pressure transients within an elastically deformable dyke (*36*). By analogy, we can make the interpretation that caldera earthquakes may generate a pressure pulse that leads to increased seismicity at the end of the dike. The communication could be two-way, although it is difficult to explain a pressure pulse from the dike towards the caldera. One possibility is that readjustment of the dike (e.g. sudden unblocking) can increase the dike volume slightly and subsequently lower the magma pressure which then translates back to the caldera. The communication may also be entirely one-way, from the caldera to the dike: smaller caldera earthquakes, and/or aseismic deformation at depth just above the magma chamber may precede a large caldera earthquake, increasing dike pressure and dike seismicity.

We explain the longer term (weeks to months scale) coupling in the form of the gradually declining rates of caldera subsidence, caldera volume change and lava eruption (Figs. 3B, 6B) with a model of a collapsing piston overlying a pressurized magma chamber. We assume that the chamber pressure and fault friction each partially support the piston weight (*24*). Drainage of magma reduces

288   the chamber pressure and causes piston subsidence (Fig. S6). This in turn raises the chamber

289   pressure, leading to a feedback loop that maintains quasi-constant pressure at the magma chamber

290   top, and drives further magma drainage. The pressure feeding the eruption drops, however, due to

291   the reduction in hydraulic head of magma over time. Kumagai et al. (37) also used a piston model to

292   explain caldera collapse at Miyakejima in 2000, but in their model no change in hydraulic head was

293   assumed and outflow rate was held constant.

294   Assuming that the time-averaged resistive force due to friction on the ring faults remains constant,

295   and that magma flow is laminar through a cylindrical pipe with radius r, and conduit length L, with

296    $L \gg r$, then

297    $$\Delta P \approx \Delta P_0 e^{-\frac{\pi \rho g r^4}{8 A \eta L} t} \qquad\qquad (1)$$

298   Where ΔP is the driving overpressure, ΔP_0 is the initial driving overpressure, ρ is the density of the

299   magma, g is gravitational acceleration, A is the cross-sectional area of the magma chamber, η is the

300   dynamic viscosity of the magma and t is time (24). We estimated ΔP_0 and the constant in the

301   exponent, assuming that the measured subsidence within the caldera represents the decrease in

302   magma chamber height with time (Fig 3B). Note, this represents a minimum estimate for ΔP_0, as

303   there may also have been dilation at depth. The model also fits the measured caldera volume

304   change (Fig. 3B) and eruption rate (Fig. 6B). This model predicts the same form of decay in flow

305   rate (exponential) as the standard 'Wadge' model of depressurisation of an overpressured magma

306   body (38), but by a different mechanism. The feedback mechanism of re-pressurisation from the

307   ongoing piston collapse enhanced the length and speed of dike propagation, and the duration of the

308   eruption. In this model, therefore, both the eruption drives the collapse and collapse drives the

309   eruption.

310
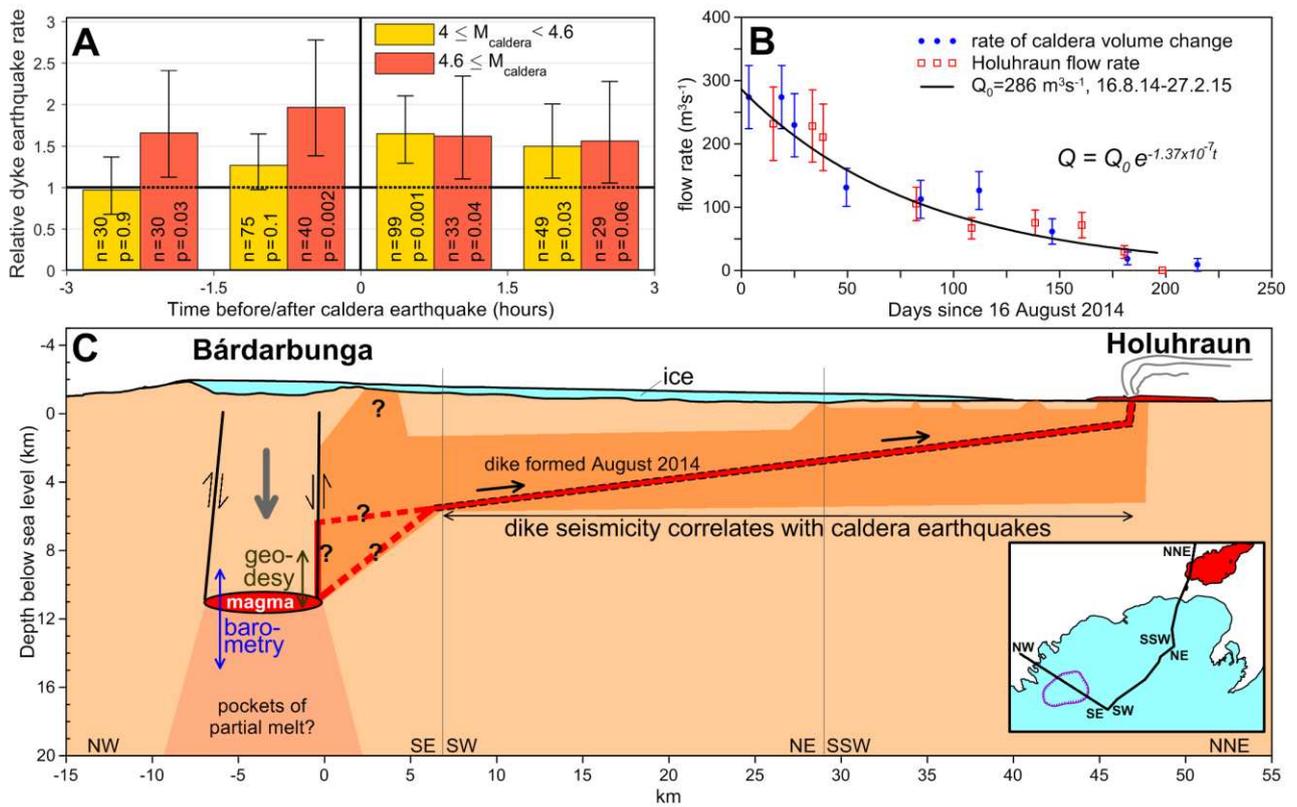
Figure 6. Caldera - magma flowpath interaction. A) Rate of dike earthquakes relative to

background levels before and after significant caldera earthquakes of magnitude >M4. The p-values

indicate the two sided significance and n is the number of earthquakes used. Error bars indicate

90% confidence intervals (24). B) Exponential model of magma flow rate constrained by caldera

GPS subsidence (*24*) compared with rate of volume change in caldera and eruption rate in

Holuhraun. The eruption stopped on Day 194 (27 February, 2015) before the driving pressure

reaches zero, as expected if the conduit becomes clogged by solidifying magma as the flow rate

drops. C) Schematic cross-section of caldera - magma chamber - pipe-like magma flow path and

eruption site after dike formation (*20, 21*). The inferred magma chamber is set at 12 km below

bedrock caldera floor. It is possible that magma ascended first along the ring fault before forming

the dyke above 6-10 km depth. We indicate the constraints on depth to magma chamber from

geobarometry with a blue arrow and from geodesy with a green arrow.

323

Overview and implications

Table 1 contextualizes the key features of the 2014-15 Bardarbunga collapse with respect to those of the seven collapses instrumentally monitored to date. The areal extent of the Bardarbunga collapse (110 km^2) is the largest yet observed historically and is comparable to that associated with major silicic eruptions in the geological record (6). The total subsidence (65 m) is one to two orders of magnitude smaller than all past collapses listed here, but the large area means that it has the fourth largest collapse volume (1.8 km^3) overall. The erupted volume (1.4 km^3) is the largest of the observed mafic collapses so far, although considerable uncertainty surrounds the volumes associated with the collapse of Fernandina. In volume terms, both the silicic eruptions and collapses of Katmai and Pinatubo were twice to six times larger. The cumulative seismic energy release at Bardarbunga (25 x 10^{13} J, see Table 1) is dwarfed by that of Katmai (1600 x 10^{13} J) and similar to Miyakejima (22 x 10^{13} J), despite the much smaller area of the latter (1.9 km^2). This is explained by the much greater subsidence at Miyakejima (>1600 m). The gradual collapse of Bardarbunga had the second longest duration (190 days) yet recorded. Only the duration of collapse at Tolbachik (515 days) exceeds it. Finally, Bardarbunga has the longest confirmed length of an associated lateral intrusion (48 km) and the longest distance to the main vent (40 km).

Volcano	Year	Magma	Maximum subsidence (m)	Collapse Duration (days)	Collapse Area (km²)	Collapse Volume (km³)	Reservoir Depth (km)	Intrusion Volume (km³) [a]	Erupted Volume (km³) [b]	Total Magma Volume (km³)	Distance to Vent [c] (km)	Intrusion Length [d] (km)	Seismic Energy (x 10¹³ J) [e]	Max. EQ [f]
Bardarbunga	2015	Basalt	~ 61	150	110	1.8	11-16	0.5	1.5	2	46	48	25	5.4
La Reunion	2007	Basalt	~ 450	2	0.82	0.1	2-3	0.02	0.14	0.16	7	7	?	3.2
Miyakejima	2000	Basalt	*~ 1600*	40	1.9	0.6	4-7	1.2	0.01	1.21	5.6	35	22	5.6
Tolbachik	1976	Basalt	> 500	**515**	2.5	0.35	4-6?	?	1.2	> 1.2	28	~ 45	?	2.9
Fernandina	1969	Basalt	~ 350	12	7	2	?	?	0.2	> 0.2	10.5?	10.5?	2	5.2
Katmai	1912	Rhyolite	> 1300	3	8.8	*5.5*	2-5	?	*13.5*	> 13.5	10	10	*1600*	*7*
*Pinatubo**	*1991*	*Dacite*	*~ 900*	*2*	*4*	*2*	*7-11*	*?*	*4.5*	*4.5*	*1*	*4*	*2*	*5.7*

Table 1: Instrumentally-monitored caldera collapses since 1900 AD.

* Note that all caldera collapses <u>except Pinatubo</u> formed in association with lateral withdrawal and intrusion of magma.

344 **References for data:** ***Bardarbunga:*** (*20*); this study; ***La Reunion:*** (*12,16,44-46*); ***Miyakejima:*** (*2, 11, 34, 47-*
345 *49*); ***Tolbachik:*** (*50-53*); ***Fernandina:*** (*2, 9, 54*); ***Katmai:*** (*35, 41, 55*); ***Pinatubo:*** (*2, 15, 42, 43, 56*)

346 [a] Intrusion volume values are typically constrained by inversions of data from geodetic networks, and so are available
347 only for the most recent events.

348 [b] Erupted volumes are given as Dense Rock Equivalent (DRE) – i.e. with porosity removed.

349 [c] Distance measured from center of caldera to most distant known vent active during collapse.

350 [d] Estimated horizontal length of the intrusion, from locations of seismicity and/or inversions of geodetic data in all
351 cases except Katmai. For Katmai and Fernandina, intrusion length is estimated as the distance from caldera to vent
352 and is hence a minimum value.

353 [e] Cumulative seismic energy release calculated by converting the cumulative scalar moments (M_0) by using a factor of
354 5×10^{-5} (from energy-moment relationship determined by Kanamori et al. (*57*))

355 [f] Maximum earthquake magnitude associated with caldera formation. Magnitude determined from surface waves,
356 Ms, is given for Tolbachik (*53*), Katmai (*35*) and Fernandina (*54*). For La Reunion, M_d is used (*12, 44*). For Miyakejima
357 and Bardarbunga, the maximum moment magnitude (M_w) for collapse-related VLP events is given (*34, 58*, this study).

358

359 Our data and modelling show that withdrawal and eruption of magma triggered the collapse at

360 Bardarbunga. For the likely depth to diameter ratio of the magma reservoir, the critical volume

361 fraction required to trigger the onset of collapse (0.12-0.21) was much lower than that predicted by

362 past analytical and analogue modelling (*23, 39*). A similar inference of low critical volume fractions

363 at La Reunion and Miyakejima (*16*) was explained as a consequence of the reactivation of pre-

364 existing ring faults, a proposition in line with our observations and analysis of the Bardarbunga

365 collapse.

366 Nonetheless, we also show that there is a tight mechanical interplay between collapse and eruption

367 throughout the process once collapse has started, with eruption driving collapse and vice versa on

368 both hourly and eruption-long time scales. For the longer time-scale coupling, the results also show

369 that the physical properties of both the magma chamber roof and the magma pathway regulate

370 caldera collapse and magma outflow rate. Consequently, collapse at Bárdarbunga occurred

371 gradually and at a steadily (exponentially) declining rate. This is a very similar pattern to that

372 inferred for the 1968 Fernandina collapse (*2, 16*). In contrast to some model predictions (*40*) and to

373 the 2007 collapse of Piton de la Fournaise (*16*), we found no evidence for rapid and sustained

374 pressure increase in the magma chamber as a result of collapse, possibly due to substantial ductile

375 behavior of the roof of the larger and deeper Bardarbunga magma chamber (*13*, *16*).

376 The question of whether or to what extent our understanding of caldera collapse at mafic volcanoes

377 such as Bardarbunga is transferrable to large silicic systems remains an open one. On the one hand

378 the gradual nature of collapse at Bardarbunga and Fernandina contrasts with the highly punctuated

379 collapse style inferred during explosive silicic eruptions like Katmai and Pinatubo (*2*, *41*). In

380 addition, collapse at silicic volcanoes is generally considered to be triggered by eruption through a

381 central vent rather than through the lateral withdrawal mechanism seen at Bardarbunga. On the

382 other hand, of the two instrumentally monitored silicic collapses, the most silicic, Katmai was also

383 clearly associated with a lateral withdrawal. This mechanism could therefore be more widespread at

384 silicic calderas than commonly considered. In addition, the locations and mechanisms of the large,

385 apparently collapse-related earthquakes interpreted to denote punctuated collapses of Katmai and

386 Pinatubo are poorly constrained, such that a regional tectonic origin for them cannot be precluded

387 (*15*, *35*, *42*, *43*). Consequently, Bardarbunga 2014-15 provides our clearest picture yet of how

388 caldera collapse can be triggered during large eruptions, and how the dynamics of the subterranean

389 magma flow path and the interaction with magma reservoir pressure regulates eruption rates and the

390 rate of collapse.

References

1. M. Branney, V. Acocella, "Calderas" in *The Encyclopedia of Volcanoes,* H. Sigurdsson, B. Houghton, H. Rymer, Eds. (Academic Press, Academic Press, Heidelberg, Amsterdam, Boston, ed. 2, 2015), pp. 229-315.

2. J. Stix, T. Kobayashi, Magma dynamics and collapse mechanisms during four historic caldera-forming events. *J. Geophys. Res.* **113**, JB005073 (2008).

3. A. R. McBirney, A historical note on the origin of calderas. *J. Volcanol. Geotherm. Res.* **42**, 303-306 (1990).

4. R. S. J. Sparks, P.W. Francis, R. D. Hamer, R. J. Pankhurst, L. O. O'callaghan, R. S. Thorpe, R. Page, Ignimbrites of the Cerro Galán caldera, NW Argentina. *J. Volcanol. Geotherm. Res.* **24**, 205-248 (1985).

5. T. H. Druitt, R. S. J. Sparks, On the formation of calderas during ignimbrite eruptions. *Nature* **310**, 679-681 (1984).

6. P. W. Lipman, Subsidence of ash-flow calderas: relation to caldera size and magma-chamber geometry. *Bull. Volc.*, **59**, 198-218 (1997).

7. V. Acocella, Understanding caldera structure and develpoment: an overview of analogue models compared to natural calderas. *Earth Sci. Rev.*, **125**, 125-160 (2007).

8. O. Roche, T. H. Druitt, O. Merle, Experimental study of caldera formation. *J. Geophys. Res.* **105**, 395-416 (2001).

430 9. T. Simkin, K. A. Howard, Caldera collapse in the Galapagos Islands, 1968: The largest known collapse since
431 1912 followed a flank eruption and explosive volcanism within the caldera. *Science* **169**, 429–437 (1970).

432 10. S. A. Fedotov, Y. K. Markhinin, *The Great Tolbachik Fissure Eruption. Geological and Geophysical Data*
433 *1975-1976.* (Cambridge University Press, Cambridge, 2011).

434 11. N. Geshi, T. Shimano, S. Chiba, Caldera collapse during the 2000 eruption of Miyakejima Volcano, Japan.
435 *Bull. Volcanol*. **64**, 55-68 (2002).

436 12. T. Staudacher, V. Ferrazzini, A. Peltier, P. Kowalski, P. Boissier, P. Catherine, F. Lauret, F. Massin, The
437 April 2007 eruption and the Dolomieu crater collapse, two major events at Piton de la Fournaise (La
438 Réunion Island, Indian Ocean). *J. Volcanol. Geotherm. Res*. **184**, 126-137 (2009).

439 13. E. P. Holohan, M. P. J. Schöpfer, J. J. Walsh, J. J. Stress evolution during caldera collapse. Earth Planet.
440 Sc. Lett. **421**, 139-151 (2015).

441 14. K. V. Cashman, G. Giordano, Calderas and magma reservoirs. *J. Volcanol. Geotherm. Res*. **288**, 28-45
442 (2014).

443 15. J. Battaglia, C. H. Thurber, J.-L. Got, C. A. Rowe, R A. White, Precise relocation of earthquakes following
444 the 15 June 1991 eruption of Mount Pinatubo (Philippines). *J. Geophys. Res*. **109**, B7 (2004).

445 16. L. Michon, F. Massin, V. Famin, V. Ferrazzini, G. Roult, Basaltic calderas: Collapse dynamics, edifice
446 deformation, and variations of magma withdrawal. *J. Geophys. Res*. **116**, B3 (2011).

447 17. H. Björnsson, P. Einarsson, Volcanoes beneath Vatnajökull, Iceland: evidence from radio-echo sounding,
448 earthquakes and jökulhlaups. *Jokull* **40**, 147-148 (1990).

449 18. M. T. Gudmundsson, T. Högnadóttir, Volcanic systems and calderas in the Vatnajökull region, central
450 Iceland, constraints on crustal structure from gravity data. Journal of Geodynamics, 43, 153-169 (2007).

451 19. T. Thordarson, G. Larsen, Volcanism in Iceland in historical time: Volcano types, eruption styles and
452 eruption history. *J. Geodyn*. **43**, 118-152 (2007).

453 20. F. Sigmundsson, A. Hooper, S. Hreinsdóttir, K. S. Vogfjörd, B. G. Ófeigsson, E. R. Heimisson, S. Dumont,
454 M. Parks, K. Spaans, G. B. Gudmundsson, V. Drouin, T. Árnadóttir, K. Jónsdóttir, M. T. Gudmundsson, T.
455 Högnadóttir, H. M. Fridriksdóttir, M. Hensch, P. Einarsson, E. Magnússon, S. Samsonov, B. Brandsdóttir, R.
456 S. White, T. Ágústsdóttir, T. Greenfield, R. G. Green, A. R. Hjartardóttir, R. Pedersen, R. A. Bennett, H.
457 Geirsson, P. C. La Femina, H. Björnsson, F. Pálsson, E. Sturkell, C. J. Bean, M. Möllhoff, A. K. Braiden, E. P. S.
458 Eibl, Segmented lateral dyke growth in a rifting event at Bárðarbunga volcanic system. *Nature* **517**, 191-195
459 (2015).

460 21. T. Ágústsdóttir, J. Woods, T. Greenfield, R. G. Green, R. S. White, T. Winder, B. Brandsdóttir, S.
461 Steinthórsson, H. Soosalu, Strike-slip faulting during the 2014 Bárðarbunga-Holuhraun dike intrusion,
462 central Iceland. *Geophys. Res. Lett*. (accepted). DOI: 10.1002/2015GL067423

463 22. S. R. Gíslason, G. Stefánsdóttir, M. A. Pfeffer, S. Barsotti, Th. Jóhannsson, I. Galeczka, E. Bali, O.
464 Sigmarsson, A. Stefánsson, N. S. Keller, A. Sigurdsson, B. Bergsson, B. Galle, V. C. Jacobo, S. Arellano, A.
465 Aiuppa, E. S. Eiríksdóttir, S. Jakobsson, G. H. Gudfinnsson, S. A. Halldórsson, H. Gunnarsson, B. Haddadi, I.
466 Jónsdóttir, Th. Thordarson, M. Riishuus, Th. Högnadóttir, T. Dürig, G. B. M. Pedersen, A. Höskuldsson, M. T.

467 Gudmundsson, Environmental pressure from the 2014–15 eruption of Bárðarbunga volcano, Iceland.
468 *Geochem. Perspect. Lett*., **1**, 84-93 (2015).

469 23. O. Roche, O., T. H. Druitt, Onset of caldera collapse during ignimbrite eruptions. Earth Planet. Sci. Lett.,
470 **191**(3), 191-202 (2001).

471 24. Materials and methods are available as supplementary materials on Science Online.

472 25. J. Browning, A. Gudmundsson, Surface displacements resulting from magma-chamber roof subsidence,
473 with application to the 2014-2015 Bardarbunga-Holuhraun volcanotectonic episode in Iceland. *J. Volcanol.*
474 *Geotherm. Res*. **308**, 82-98 (2015).

475 26. H. Björnsson, Hydrology of ice caps in volcanic regions. Soc. Sci. Isl. 45, 139pp (1988).

476 27. E. P. Holohan, V. R. Troll, B. Van Wyk de Vries, J. J. Walsh, T. R. Walter, Unzipping Long Valley: an
477 explanation for vent migration during an elliptical ring fracture eruption. *Geology* **36**, 323-326 (2008).

478 28. E. P. Holohan, T. R. Walter, M.P. Schöpfer, J. J. Walsh, B. Wyk de Vries, V. R. Troll, Origins of oblique-slip
479 faulting during caldera subsidence. J. Geophys. Res. **118**(4), 1778-1794 (2013).

480 29. C. Clough, H. Maufe, E. Baley, The cauldron subsidence of Glen-Coe, and the associated igneous
481 phenomena. Q.J.Soc. Lond. **65**, 611–678 (1909).

482 30. H. Bathke, M. Nikhoo, E.P. Holohan, T.R. Walter, Insights into the 3D architecture of an active caldera
483 ring-fault at Tendürek volcano through modeling of geodetic data. Earth. Planet. Sci. Lett. **422**:157-168
484 (2015).

485 31. A. Fichtner, H. Tkalcic, Insights into the kinematics of a volcanic caldera drop: Probabilistic finite-source
486 inversion of the 1996 Bardarbunga, Iceland, earthquake. *Earth Planet. Sc. Lett*. **297**, 607-615 (2010).

487 32. B. Riel, P. Milillo, M. Simons, P. Lundgren, H. Kanamori, H., S. Samsonov, The collapse of Bárðarbunga
488 Caldera, Iceland. *Geophys. J. Int*. **202**, 446-453 (2015).

489 33. S. Cesca, A. T. Sen, T. Dahm, Seismicity monitoring by cluster analysis of moment tensors. *Geophys. J.*
490 *Int*. **196**, 1813-1826 (2013).

491 34. A. Shuler, G. Ekström, M. Nettles, Physical mechanisms for vertical-CLVD earthquakes at active
492 volcanoes. J. Geophys. Res. **118**(4), 1569-1586 (2013).

493 35. K. Abe, Seismicity of the caldera-making eruption of Mount Katmai, Alaska in 1912. *B. Seismol. Soc. Am*.
494 **82**, 175-191 (1992).

495 36. C. P. Montagna, H. M. Gonnermann, Magma flow between summit and Pu`u `O`o at Kilauea Volcano,
496 Hawaii. *Geochem. Geophy. Geosy.* **14**, 2232–2246 (2013).

497 37. H. Kumagai, T. Ohminato, M. Nakano, M. Ooi, A. Kubo, H. Inoue, J. Oikawa, Very-long-period seismic
498 signals and caldera formation at Miyake Island, Japan. Sci. 293, 687-690 (2001).

499 38. G. Wadge, Steady state volcanism: evidence from eruption histories of polygenetic volcanoes.
500 J. Geophys. Res. **87**, B5: 4035-4049 (1982).

501 39. A. Geyer, A. Folch, J. Martí, Relationship between caldera collapse and magma chamber withdrawal: an
502 experimental approach. J Volcanol. Geotherm. Res. **157**, 375-386 (2006).

503 40. A. Folch, J. Marti, Time-dependent chamber and vent conditions during explosive caldera-forming
504 eruptions. *Earth Planet. Sc. Lett.* **280**, 246-253 (2009).

505 41. W. Hildreth, J. Fierstein, Katmai volcanic cluster and the great eruption of 1912. *Geophys. J. Int.* **112**,
506 446-453 (2000).

507 42. B. C. Bautista, M. L. P. Bautista, R. S. Stein, E. S. Barcelona, R. S. Punongbayan, E. P. Laguerta, A. R.
508 Rasdas, G. Ambubuyog, E. Q. Amin, "Relationship of regional and local structures to Mount Pinatubo
509 activity" in *Fire and Mud: Eruptions and Lahars of Mount Pinatubo, Philippines. PHIVOLCS*, C. G. Newhall, R.
510 S. Punongbayan, Eds. (University of Washington Press, Quezon City, 1996), pp. 351-370.

511 43. J. Mori, R. A. White, D. H. Harlow, P. Okubo, J. A. Power, R. P. Hoblitt, E. P. Laguerta, A. Lanuza, B. C.
512 Bautista, "Volcanic earth quakes following the 1991 climactic eruption of Mount Pinatubo: strong seismicity
513 during a waning eruption" in *Fire and Mud: Eruptions and Lahars of Mount Pinatubo, Philippines. PHIVOLCS*.
514 C. G. Newhall, R. S. Punongbayan, Eds. (University of Washington Press, Quezon City, 1996), pp. 339-350.

515 44. L. Michon, T. Staudacher, V. Ferrazzini, P. Bachèlery, J. Marti, April 2007 collapse of Piton de la
516 Fournaise: a new example of caldera formation. *Geophys. Res. Lett.*, **34**(21) (2007).

517 45. F. R. Fontaine, G. Roult, L. Michon, G. Barruol, A. Di Muro, The 2007 eruptions and caldera collapse of
518 the Piton de la Fournaise volcano (La Reunion Island) from tilt analysis at a single very broadband seismic
519 station. *Geophys. Res. Lett.* **41**, 2803-2811 (2014); published online EpubApr 28 (10.1002/2014GL059691).

520 46. A. Di Muro, N. Metrich, D. Vergani, M. Rosi, P. Armienti, T. Fougeroux, E. Deloule, I. Arienzo, L. Civetta,
521 The Shallow Plumbing System of Piton de la Fournaise Volcano (La R,union Island, Indian Ocean) Revealed
522 by the Major 2007 Caldera-Forming Eruption. *J. Petrol.* **55**, 1287-1315 (2014); published online EpubJul
523 (10.1093/petrology/egu025).

524 47. T. Kaneko, A. Yasuda, T. Shimano, S. Nakada, T. Fujii, T. Kanazawa, A. Nishizawa, Y. Matsumoto,
525 Submarine flank eruption preceding caldera subsidence during the 2000 eruption of Miyakejima Volcano,
526 Japan. *Bull. Volcanol.* **67**, 243-253 (2005); published online EpubMar (10.1007/s00445-004-0407-1).

527 48. M. Amma-Miyasaka, M. Nakagawa, S. Nakada, Magma plumbing system of the 2000 eruption of
528 Miyakejima Volcano, Japan. *Bull. Volcanol.* **67**, 254-267 (2005); published online EpubMar
529 (10.1007/s00445-004-0408-0).

530 49. T. Nishimura, S. Ozawa, M. Murakami, T. Sagiya, T. Tada, M. Kaidzu, M. Ukawa, Crustal Deformation
531 caused by magma migration in the northern Izu Islands, Japan. *Geophys. Res. Lett.* **28**, 3745-3748 (2001);
532 published online EpubOct 1 (Doi 10.1029/2001gl013051).

533 50. S. A. Fedotov, L. B. Slavina, S. L. Senyukov, M. S. Kuchay, Seismic processes and migration of magma
534 during the Great Tolbachik Fissure Eruption of 1975-1976 and Tolbachik Fissure Eruption of 2012-2013,
535 Kamchatka Peninsula. *Izv. Atmos. Ocean Phy.* **51**, 667-687 (2015); published online EpubDec
536 (10.1134/S000143381507004x).

537 51. S. A. Fedotov, I. S. Utkin, L. I. Utkina, The Peripheral Magma Chamber of Ploskii Tolbachik, a Kamchatka
538 Basaltic Volcano: Activity, Location and Depth, Dimensions, and their Changes Based on Magma Discharge
539 Observations. *J. Volcanol. Seismol.* **5**, 369-385 (2011); published online EpubDec
540 (10.1134/S0742046311060042).

541 52. P. Doubik, B. E. Hill, Magmatic and hydromagmatic conduit development during the 1975 Tolbachik
542 Eruption, Kamchatka, with implications for hazards assessment at Yucca Mountain, NV. *J. Volcanol.*
543 *Geotherm. Res*. **91**, 43-64 (1999); published online EpubJul (Doi 10.1016/S0377-0273(99)00052-9).

544 53. S.A. Fedotov, A. M. Chirkov, N.A. Gusev,G. N. Kovalev, Y. B. Slezin, The large fissure eruption in the
545 region of Plosky Tolbachik volcano in Kamchatka, 1975–1976. *Bull. Volcanol*. **43,** 47-60 (1980).

546 54. J. Filson, T. Simkin, L. K. Leu, Seismicity of a caldera collapse: Galapagos Islands 1968. J. Geophys. Res.,
547 **78**(35), 8591-8622 (1973).

548 55. J. E. Hammer, M. J. Rutherford, W. Hildreth, Magma storage prior to the 1912 eruption at Novarupta,
549 Alaska. *Contrib. Mineral. Petr*. **144**, 144-162 (2002); published online EpubNov (10.1007/s00410-002-0393-
550 2).

551 56. M. J. Rutherford, J. D. Devine, in *Fire and Mud: Eruptions and Lahars of Mount Pinatubo, Philippines* C.
552 G. Newhall, R. S. Punongbayan, Eds. (Philippine Institute of Volcanology and Seismology & University of
553 Washington Press, Quezon City, Seattle & London, 1996), pp. 751–766.

554 57. H. Kanamori, J. Mori, E. Hauksson, T. H. Heaton, L. K. Hutton, L. M. Jones, Determination of earthquake
555 energy release and ML using TERRAscope. Bull. . Seismol. Soc. Am., **83**(2), 330-346 (1993).

556 58. M. Kikuchi, Y. Yamanaka, K. Koketsu, Source Process of the Long-period Seismic Pulses Associated with
557 the 2000 Eruption of Miyakejima Volcano and its Implications. J. Geograph. Tokyo **110**(2), 204-216 (2001).

558 59. M. T. Gudmundsson, T. Hognadottir, A. B. Kristinsson, S. Gudbjornsson, Geothermal activity in the
559 subglacial Katla caldera, Iceland 1999-2005, studied with radar altimetry. *Ann. Glacio*. **45**, 66-72 (2007).

560 60. C. Mätzler, Microwave permittivity of dry snow. *IEEE Trans. Geosci. Remote Sens*. **34**, 573-581 (1996).

561 61. C. Rossi, C. Minet, T. Fritz, M. Eineder, R. Bamler, Temporal monitoring of subglacial volcanoes with
562 TanDEM-X—Application to the 2014–2015 eruption within the Bárðarbunga volcanic system, Iceland.
563 Remote Sens. Environ. 181, 186-197 (2016)

564 62. T. Johannesson, H. Björnsson, E. Magnússon, S. Guðmundsson, F. Pálsson, O. Sigurðsson, T.
565 Thorsteinsson, E. Berthier, Ice-volume changes, bias estimation of mass-balance measurements and
566 changes in subglacial lakes derived by lidar mapping of the surface of Icelandic glaciers. *Ann. Glacio.* **54**, 63-
567 74 (2013).

568 63. E. Magnusson, F. Palsson, H. Bjornsson, S. Gudmundsson, Removing the ice cap of Oraefajokull central
569 volcano, SE-Iceland: Mapping and interpretation of bedrock topography, ice volumes, subglacial troughs
570 and implications for hazards assessments. *Jokull* **62**, 131-150 (2012).

571 64. H. Bjornsson, F. Pálsson, M. T. Gudmundsson, *Vatnajokull, Northwest Part, 1:100 000: Bedrock*
572 *topography*, Landsvirkjun and Science Institute, University of Iceland, 1992.

573 65. A. H. Jarosch, Icetools: A full Stokes finite element model for glaciers. *Comput. Geosci*. **34**, 1004-1014
574 (2008).

575 66. J. W. Glen, The Creep of Polycrystalline Ice. *P. Roy. Soc. A-Math. Phy*. **228**, 519-538 (1955).

576   67. K. M. Cuffey, W. S. B. Paterson, *The Physics of Glaciers.* (Elsevier Butterworth-Heinemann, Burlington,
577   ed. 4, 2010).

578   68. C. E. Lesher, F. J. Spera, "Thermodynamic and Transport Properties of Silicate Melts and Magma" in *The*
579   *Encyclopedia of Volcanoes*, H. Sigurdsson, B. Houghton, H. Rymer, Eds. (Academic Press, Academic Press,
580   Heidelberg, Amsterdam, Boston, ed. 2, 2015), pp. 113-141.

581   69. R. Bödvarsson, S. T. Rögnvaldsson, R. Slunga, E. Kjartansson, The SIL data acquisition system—at present
582   and beyond year 2000. *Phys. Earth Planet. Inter*. **113**, 89-101 (1999).

583   70. R. Slunga, S. T. Rögnvaldsson, R. Bödvarsson, Absolute and relative locations of similar events with
584   application to microearthquakes in southern Iceland. *Geophys. J. Int*. **123**, 409–419 (1995).

585   71. S. Th. Rögnvaldsson, R. Slunga, Routine fault plane solutions for local networks: a test with synthetic
586   data. Bull. Seism. Soc. Am. **83**.4, 1232-1247 (1993).

587   72. R. Stefánsson, R. Böðvarsson, R. Slunga, P. Einarsson, S. Jakobsdóttir, H. Bungum, S. Gregersen, J.
588   Havskov, J. Hjelme, H. Korhonen, Earthquake prediction research in the South Iceland seismic zone and the
589   SIL project. *Bull. Seism. Soc. Am*. **83**, 696–716 (1993).

590   73. S., A., R. Cesca, T. Dahm, Discrimination of induced seismicity by full moment tensor inversion and
591   decomposition. *J. Seimsol*. **17**, 147-163 (2013).

592   74. P. A. Rosen, S. Hensley, I. R. Joughin, F. K. Li, S. N. Madsen, E. Rodriguez, R. M. Goldstein, Synthetic
593   aperture radar interferometry, presented at *Proceedings of the IEEE,* 2000 (unpublished).

594   75. B. Kampes, Delft Object-oriented Radar Interferometric Software: User's Manual and Technical
595   Documentation v4.02, presented at *Delft Technical University*, 1999 (unpublished).

596   76. Y. Y. Kagan, 3-D rotation of double-couple earthquake sources. *Geophys. J. Int*. **106**, 709–716 (1991).

597   77. R. M. Goldstein, C. L. Werner, Radar interferogram filtering for geophysical applications. *Geophys. Res.*
598   *Lett*. **25**, 4035-4038 (1998).

599   78. C. W. Chen, H. A. Zebker, Two-dimensional phase unwrapping with use of statistical models for cost
600   functions in nonlinear optimization. *J. Opt. Soc. Am. A Opt. Image. Sci. Vis*. **18**, 338-351 (2001).

601   79. Y. Okada, Internal deformation due to shear and tensile faults in a half-space. *B. Seismol. Soc. Am*. **82**,
602   1018-1040 (1992).

603   80. A. Hooper, J. Pietrzak, W. Simons, H. Cui, R. Riva, M. Naeije, A. Terwisscha van Scheltinga, E. Schrama, G.
604   Stelling, A. Socquet, Importance of horizontal seafloor motion on tsunami height for the 2011 Mw=9.0
605   Tohoku-Oki earthquake. *Earth Planet. Sc. Lett*. **361**, 469-479 (2013).

606   81. C. E. Ford, D. G. Russell, J. A. Craven, M. R. Fisk, Olivine-liquid equilibria: Temperature, pressure and
607   composition dependence of the crystal/liquid cation partition coefficients for Mg, Fe2+, Ca and Mn. *J.*
608   *Petrol*. **24**, 256-266 (1983).

609   82. H. J. Yang, R. J. Kinzler, T. L. Grove, Experiments and models of anhydrous, basaltic olivine-plagioclase-
610   augite saturated melts from 0.001 to 10 kbar. *Contrib. Mineral. Petr*. **124**, 1-18 (1996).

611   83. G. H. Gudfinnsson, D. C. Presnall, A pressure-independent geothermometer for primitive mantle melts.
612   *J. Geophys. Res*. **106**, B8 (2001).

613   84. K. D. Putirka, Thermometers and barometers for volcanic systems. *Rev. Mineral. Geochem*. **69**, 61-120
614   (2008).

615   85. Y. Kawakami, J. Yamamoto, H. Kagi, Microraman densimeter for CO_2 inclusions in mantle derived
616   minerals. *Appl. Spectrosc*. **57**, 1333-1339 (2003).

617   86. M.R. Burton, P. Allard, F. Mure, A. La Spina, Magmatic gas composition reveals the
618   source depth of slug-driven Strombolian explosive activity, *Science*, **317**, 5835, 227-230 (2007),
619   doi:10.1126/science.1141900.

620
621   87. A. Aiuppa, C. Federico, G. Giudice, S. Gurrieri, Chemical mapping of a fumarolic field: La Fossa Crater,
622   Vulcano Island (Aeolian Islands, Italy), *Geophys. Res. Lett.*, **32** (13) (2005), p. L13309
623   http://dx.doi.org/10.1029/2005GL023207

624   88. P.-J. Gauthier, O. Sigmarsson*,* M. Gouhier*,* B. Haddadi, and S. Moune, Elevated gas flux and trace metal
625   degassing from the 2014–2015 fissure eruption at the Bárðarbunga volcanic system, Iceland, *J. Geophys.*
626   *Res. Solid Earth,* **121**, (2016) doi:10.1002/2015JB012111.

627   89. E. Bali, O. Sigmarsson, S. Jakobsson, H. Gunnarsson, Volatile budget of the Nornahraun eruption in the
628   Bárðarbunga system, Iceland. Geophysical Research Abstracts Vol. 17, EGU2015-5757, 2015 EGU General
629   Assembly (2015). http://meetingorganizer.copernicus.org/EGU2015/EGU2015-5757.pdf

630   90. A. Burgisser, M. Alletti, B. Scaillet, Simulating the behavior of volatiles belonging to the C–O–H–S
631   system in silicate melts under magmatic conditions with the software D-Compress, *Comput. Geosci.*, **79**, 1–
632   14.

633   91. D. O. Potyondy, P. A. Cundall, A bonded particle model for rock. *Int. J. Rock Mech. Min.* **41**, 1329-1364
634   (2004).

635   92. D. Mas Ivars, M. E. Pierce, C. Darcel, J. Reyes-Montes, D. O. Potyondy, R. P. Young, P. A. Cundall, The
636   synthetic rock mass approach for jointed rock mass modelling. *Int. J. Rock Mech. Min*. **48**, 219-244 (2011).

637   93. Itasca Consulting Group, Inc*. PFC2D - Particle Flow Code in Two-Dimensions, Ver. 5.0.* Minneapolis,
638   Itasca (2014).

639   94. K. Mogi, Relations between the eruptions of various volcanoes and the deformations of the ground
640   surfaces around them. *B. Earthq. Res. Inst. Univ. Tokyo* **36**, 99–134 (1958).

641   95. M. Ripepe, D. Delle Donne, R. Genco, G. Maggio, M. Pistolesi, E. Marchetti, G. Lacanna, G. U. P. Poggi,
642   Volcano seismicity and ground deformation unveil the gravity-driven magma discharge dynamics of a
643   volcanic eruption. *Nat. Commun*. **6** (2015).

644   96. Y. Bottinga, D. Weill, The viscosity of magmatic silicate liquids: a model for calculation. *Am. J. Sci*. **272**,
645   438–475 (1972).

646

647 **One page summary:**

648 **Gradual caldera collapse at Bárdarbunga volcano, Iceland,**

649 **regulated by lateral magma outflow**

650 Magnús T. Gudmundsson[1], Kristín Jónsdóttir[2], Andrew Hooper[3], Eoghan P. Holohan[4,5], Saemundur

651 A. Halldórsson[1], Benedikt G. Ófeigsson[2], Simone Cesca[4], Kristín S. Vogfjörd[2], Freysteinn

652 Sigmundsson[1], Thórdís Högnadóttir[1], Páll Einarsson[1], Olgeir Sigmarsson[1,6], Alexander H. Jarosch[1],

653 Kristján Jónasson[7], Eyjólfur Magnússon[1], Sigrún Hreinsdóttir[8], Marco Bagnardi[3], Michelle M.

654 Parks[1], Vala Hjörleifsdóttir[9], Finnur Pálsson[1], Thomas R. Walter[4], Martin P.J. Schöpfer[10], Sebastian

655 Heimann[4], Hannah I. Reynolds[1], Stéphanie Dumont[1], Eniko Bali[1], Gudmundur H. Gudfinnsson[1],

656 Torsten Dahm[4], Matthew Roberts[2], Martin Hensch[2], Joaquín, M.C. Belart[1], Karsten Spaans[3],

657 Sigurdur Jakobsson[1], Gunnar B. Gudmundsson[2], Hildur M. Fridriksdóttir[1,2], Vincent Drouin[1],

658 Tobias Dürig[1], Gudfinna Adalgeirsdóttir[1], Morten S. Riishuus[1], Gro B.M. Pedersen[1], Tayo van

659 Boeckel[1], Björn Oddsson[11], Melissa A. Pfeffer[2], Sara Barsotti[2], Baldur Bergsson[2], Amy Donovan[12],

660 Mike R. Burton[13], Alessandro Aiuppa[14]

661 **INTRODUCTION:** The Bárdarbunga caldera volcano in central Iceland collapsed from August

662 2014 – February 2015 during the largest eruption in Europe since 1784. An ice-filled subsidence

663 bowl 8 x11 km wide and up to 65 m deep developed, while magma drained laterally for 45 km

664 along a subterranean path and erupted as a major lava flow northeast of the volcano. Our data

665 provide unprecedented insight into of the workings of a collapsing caldera.

666 **RATIONALE:** Collapses of caldera volcanoes are, fortunately, not very frequent, as they are often

667 associated with very large volcanic eruptions. On the other hand, the rarity of caldera collapses

668 limits insight into this major geological hazard. Since the formation of Katmai caldera in 1912,

669 during the 20th century's largest eruption, only five caldera collapses are known to have occurred

670 before that at Bárdarbunga. We used aircraft-based altimetry, satellite photogrammetry, radar

671 interferometry, ground-based GPS, evolution of seismicity, radio-echo soundings of ice thickness,

672 ice flow modeling and geobarometry to describe and analyze the evolving subsidence geometry, its

673 underlying cause, the amount of magma erupted, the geometry of the subsurface caldera ring faults

674 and the moment tensor solutions of the collapse-related earthquakes.

675 **RESULTS:** After initial lateral withdrawal of magma for some days though a magma-filled

676 fracture propagating through the Earth's upper crust, pre-existing ring faults under the volcano were

677 reactivated over the period 20-24 August, marking the onset of collapse. On August 31, the eruption

678 started and it terminated when the collapse stopped, having produced 1.5 km^3 of basaltic lava. The

679 subsidence of the caldera declined with time in a near exponential manner, in phase with the lava

680 flow rate.

681 The volume of the subsidence bowl was about 1.8 km^3. Using radio-echo soundings, we find that

682 the subglacial bedrock surface after the collapse is down-sagged with no indications of steep fault

683 escarpments. Using geobarometry, we determined the source depth of the magma to be

684 approximately 12 km and modelling of geodetic observations gives a similar result.   High precision

685 earthquake locations and moment tensor analysis of the remarkable magnitude M5 earthquake

686 series are consistent with steeply dipping ring faults. Statistical analysis of seismicity reveals

687 communication over tens of kilometers between the caldera and the dyke.

688 **CONCLUSIONS:** We conclude that interaction between the pressure exerted by the subsiding

689 reservoir roof and the physical properties of the subsurface flow path explain the gradual near

690 exponential decline of both collapse rate and the intensity of the 181-day long eruption. By

691 combining our various data sets, we show that the onset of collapse was caused by outflow of

692 magma from underneath the caldera when 12-20% of the total magma intruded and erupted had

693 flowed from the magma reservoir. However, the continued subsidence was driven by a feedback

694 between the pressure of the piston-like block overlying the reservoir, and the 47 km long magma

30

695 outflow path. Our data provide better constraints on caldera mechanisms than previously available,

696 demonstrating what caused the onset, and how both the roof overburden and the flow path

697 properties regulate the collapse.

698
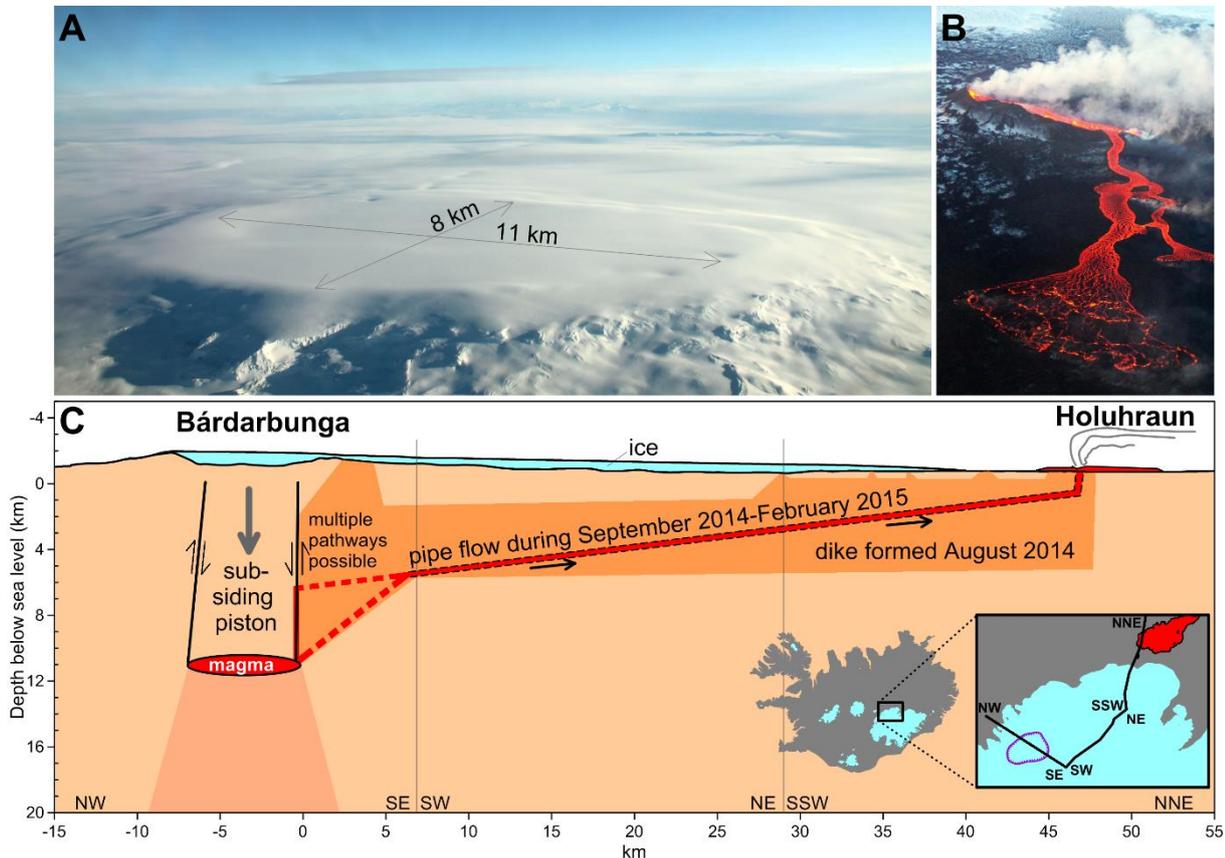
700 **The Bárdarbunga caldera and the lateral magma flowpath to the Holuhraun eruption site.**

701 (**A**) Aerial view of the ice-filled Bárdarbunga caldera on 24 October 2014, view from the north. (**B**)

702 The effusive eruption in Holuhraun, 45 km to the northeast of the caldera. (**C**) A schematic cross-

703 section through the caldera and along the lateral subterranean flow path between the magma

704 reservoir and the surface.

705

Supplementary Materials for

Gradual Caldera Collapse at Bárdarbunga Volcano, Iceland, Regulated by Lateral Magma Outflow

Magnús T. Gudmundsson,* Kristín Jónsdóttir, Andrew Hooper, Eoghan P. Holohan, Saemundur A. Halldórsson, Benedikt G. Ófeigsson, Simone Cesca, Kristín S. Vogfjörd, Freysteinn Sigmundsson, Thórdís Högnadóttir, Páll Einarsson, Olgeir Sigmarsson, Alexander H. Jarosch, Kristján Jónasson, Eyjólfur Magnússon, Sigrún Hreinsdóttir, Marco Bagnardi, Michelle M. Parks, Vala Hjörleifsdóttir, Finnur Pálsson, Thomas R. Walter, Martin P.J. Schöpfer, Sebastian Heimann, Hannah I. Reynolds, Stéphanie Dumont, Eniko Bali, Gudmundur H. Gudfinnsson, Torsten Dahm, Matthew Roberts, Martin Hensch, Joaquín, M.C. Belart, Karsten Spaans, Sigurdur Jakobsson, Gunnar B. Gudmundsson, Hildur M. Fridriksdóttir, Vincent Drouin, Tobias Dürig, Gudfinna Adalgeirsdóttir, Morten S. Riishuus, Gro B.M. Pedersen, Tayo van Boeckel, Björn Oddsson, Melissa A. Pfeffer, Sara Barsotti, Baldur Bergsson, Amy Donovan, Mike R. Burton, Alessandro Aiuppa

.

* correspondence to: mtg@hi.is

This PDF file includes:

Materials and Methods

SupplementaryText

Figs. S1 to S8

Materials and Methods

Mapping of collapse

Ice surface topography was mapped 18 times in the period September 5, 2014 to June 4, 2015 (Fig. S1). An aircraft-based system (*59*) of sub-meter differential GPS and ground clearance altimeter (4.3 GHz wave, vertical elevation accuracy ±2 m) on board the survey aircraft of Isavia, the Icelandic Civil Aviation Service (*59*) provided 13 maps (Marked as FMS on Fig. S1). Survey lines were flown at 70-120 m ground clearance, measuring 4 times/sec. (at ~15 m intervals), and included coverage of the growing geothermal ice cauldrons. Comparison with kinematic GPS ground surveys in November, February and June (accuracy ±0.3 m), as well as snow temperature models and measurements show that the reflecting surface was unaffected by accumulation of winter snow and remained at the September 2014 summer surface until October, after which it gradually migrated downwards to ~1.5 m below it by February 2015. The reflecting surface probably indicates the lower boundary of the dry snow layer where snow temperature was <0°C (*60*). A subset of this data was used by Rossi et al. (*61*) to compare with Tandem-X derived maps of the subsidence for specific dates in late 2014. Optical photogrammetry maps were made using satellite data for August 28 (Spot 6 satellite), September 20 and October 10 (Pléiades satellite). Combined, the surface data provide a record of collapse volume with time (Fig. 3B). The curve in Fig. 3B is drawn using the difference of the running average of volume obtained in three adjacent surveys. The rate of volume change obtained in this way is also used in Fig. 6B. A continuously recording GPS station (BARC) was installed on the ice-surface on September 12, 2014. This station monitored the subsidence continuously for a large part of the unrest, although snow covering the antenna lead to some data gaps. A detailed ground kinematic GPS survey within and around the caldera on June 3-10, 2015 allowed the margins of collapse to be determined. Measurements of winter accumulation in the Bárdarbunga caldera in June 2015 constrained subsidence data while a glacier surface lidar map from 2011-2012 (*62*) was used as reference surface.

Radio-echo soundings (RES)

On February 3, 2015, when over 95% of the subsidence had occurred, 45 km of RES-profiles (1-5 MHz receiver bandwidth) were measured in over-snow traverses, covering about 2/3 of the caldera floor, including a large part of the subsided area. Bedrock echoes were detected for ~90% of the measurements. Along-profile bedrock echoes in length-depth coordinates were migrated (*63*) to compensate for the width of the radar beam (~200 m). Comparison of our data with previous mapping done in 1985 (*64*) indicates that the over 60 m subsidence had not caused significant changes in ice thickness; the maximum thickness observed is close to 800 meters on both occasions.

Ice flow modelling

Assuming no basal slip ($\mathbf{v}_b$ = 0), ice deformation within the caldera has been computed using a Full-Stokes finite element model solving the standard equations (*65*). On the lateral boundaries of the model domain, no flow conditions (i.e. $\mathbf{v}$ = 0) have been defined and the model domain chosen to be sufficiently large so that the lateral boundary conditions do not influence the ice flow within the caldera. The rate factor in Glen's flow law (*66*) has been estimated by constraining the horizontal model surface velocities to fit the measured ones at the BARC GPS station for the period September 12 to February 3. This yielded A=1.6 10^{-24} $Pa^{-3}s^{-1}$ assuming the nonlinearity parameter in Glen's flow law to be n=3. This is somewhat stiffer than textbook values for temperate ice (A=2.4 10^{-24} $Pa^{-3}s^{-1}$, ref. *67*) but is to be expected in a volcanic setting

774 where the ice body contains several tephra layers. Moreover, this low value for A supports our initial
775 assumption of no basal slip. At the basal boundary, the post-collapse bed topography from the RES survey
776 has been used and the surface of each model utilized the respective surface DTM implemented as a free
777 surface within the FEM model. The ice flow modelling (Fig. S2) indicates that the ice surface subsidence was
778 almost identical to bedrock subsidence everywhere in the caldera (error <1 m) in September-October.
779 However, by the end of February the inflow of ice towards the bottom of the subsidence structure had
780 resulted in uplift of about 3 m in the center and a subsidence of 1-3 m on a circle around the uplifted
781 central part.

782

783 <u>Lava volume and flow rate</u>

784 The surface elevation of the growing Holuhraun lava flow was measured using a Theodolite from the
785 ground in September 21 2014, and with the Isavia aircraft (see above on mapping of collapse) on November
786 4 and 26, December 4 and 30 and January 21, as well as later surveys in 2015. The aircraft surveys were
787 calibrated with kinematic GPS profiling of the surface. These data give lava volumes at the time of survey,
788 providing estimates of the average magma flow rate over periods of some weeks (Fig. 6B) and a final lava
789 volume of 1.5±0.2 km^3. Nettleton gravity profiles obtained in September 2015 of the lava indicate average
790 bulk lava density of 2500±100 kg m^{-3}. Using a basaltic magma density of 2750 kg m^{-3} for pressure of 300-400
791 MPa (*68*) the equivalent volume of magma at ~12 km depth in the crust is 1.4±0.2 km^3.

792

793 <u>Relative locations of microearthquakes</u>

794 M ≤2 earthquakes at the caldera recorded at distances <100 km between August 1 and October 17 by the
795 Icelandic national seismic network, SIL (*69*) were relatively relocated using a standard 1D velocity model
796 (*70*). SIL magnitudes were calculated according to Rognvaldsson and Slunga (*71*). A double-difference
797 method was used, where absolute and relative arrival times of P and S waves determined through cross-
798 correlation of waveforms, were inverted for best locations in multiple overlapping groups (*72*). Depth is set
799 to zero at bedrock caldera floor (1.2 km above sea level, see Figs. 5 and 6). The relocated events roughly
800 follow the north and south caldera rims; mostly being outside the northern rim and ~1 km inside the
801 southern rim (Fig. 5A-B). Stability tests of relocations with subsets of events and stations indicated
802 perturbations to event latitudes, particularly on the northern rim, probably due to slow velocities inside the
803 caldera.

804 The InSAR detected subsidence associated with a M5.3 event on 18 September places the surface fault at
805 ~2.5 km inside the pre-existing topographic northern caldera rim (Fig. S7), while the seismic epicentre
806 location is just north of the northern caldera rim. Using the InSAR observation to locate the surface
807 expression for the steeply outwards dipping caldera fault, the microearthquakes were shifted southward
808 according to: *New lat = old lat * 0.883 +7.552.* The shifted locations are used in Figure 5. The shift is of the
809 same order as the absolute error in the hypocentre locations. However, besides fitting the hypocentres to
810 the InSAR-located fault it provides more consistency to S-P times from 82 events observed on an
811 accelerometer at location BARC (Fig1A) from November 2014 to February 2015.

812

813 <u>Moment tensor inversion and classification</u>

814 The steady subsidence of the caldera was accompanied by a sequence of episodic M>5 earthquakes, which
815 excited low frequency signals recorded at regional distances throughout Iceland. We performed a regional
816 moment tensor inversion for all events with M>5, adopting a full moment tensor (MT) point source
817 approximation, neglecting higher order moment tensor. The MT inversion (*73*) was performed by fitting full
818 waveforms 3-component displacements at regional distances (40-200 km), in the low frequency band 0.01-
819 0.05 Hz. We obtain centroid location, centroid depth and full MT solutions for 77 earthquakes at the
820 caldera and with M > 5. MTs were decomposed into double couple (DC), compensated linear vector dipole
821 (CLVD) and isotropic (ISO) components. Since MTs mostly differ in their DC components, we classified upon
822 the similarity of the DC orientation using a clustering algorithm (*73*) and the normalized Kagan angle (*74*) as
823 norm.

825 <u>Waveform similarity analysis and moment estimation</u>

826 To extend the interpretation of source processes to smaller events, where MT inversion becomes less
827 stable, we apply a waveform similarity analysis. The scaling of the low frequency signals of weaker events
828 and larger ones with similar waveforms is used to infer the scalar moment of smaller events (M < 5) from
829 the known moment of the larger ones, resulting from the MT inversion procedure. In this way, we are able
830 to estimate scalar moments for more than 600 events (352 with Mw > 4.0), down to a magnitude of Mw
831 3.3. These results allow tracking of the details of the temporal evolution of the moment release.

833 <u>Mechanism corrected relative location</u>

834 Moment tensor inversion provides a first estimate of centroid location and depth. A more precise location
835 can be obtained by using relative location techniques, here also favored by the high waveform similarity.
836 However, waveform-based lag-times can be affected by the dissimilarity among waveforms for the two
837 families of events. To overcome this problem, we corrected cross-correlation lag times, by using corrections
838 based upon focal mechanisms. The adopted procedure includes the computation of synthetic seismograms
839 for different observed source mechanisms, the cross-correlation of synthetic waveforms to estimate
840 fictitious time lags due to different focal mechanisms, and the inference of a time lag correction for each
841 possible focal mechanism pair. As a result, we improved epicentral locations for 227 events. In order to
842 obtain absolute locations, we combine the relative centroid locations of the largest events with the new
843 absolute epicentral locations, imposing the condition that the mean centroid locations correspond to the
844 mean absolute locations for both the northern and the southern cluster.

846 <u>Caldera-dike seismicity correlations</u>

847   The histogram shown in Figure 6A is computed using a simple model using the number of dyke
848 earthquakes in 1.5 hour bins before and after (i) 4 < M < 4.6 and (ii) M > 4.6 caldera earthquakes (61). For
849 example, the height of the fourth bar is found by assuming that the rate of dyke earthquakes during the 1.5
850 hours immediately preceding an M $\geq$ 4.6 caldera earthquake is α times the reference rate, and estimating α
851 with maximum likelihood, giving α =1.96. The plot can be read as, for example, the expected rate of dyke
852 earthquakes is increased by 96% in the time interval 1.5 hours before an M $\geq$ 4.6 caldera earthquake.

853   P-values are computed with a likelihood ratio test, and the confidence intervals are likelihood based. The
854   reference rate (equal to 1 in Fig. 6A) is the rate of earthquake occurrence in periods more than three hours
855   before or after caldera earthquakes of size M > 4. All dyke earthquakes that fall in one of the bins of Figure
856   6A together with all the dyke earthquakes in the reference periods are considered. The null hypothesis is
857   that the portion of these earthquakes that fall in the bin is binomially distributed with parameter
858   corresponding to a constant reference rate. To minimize the effect of the varying reference rate between
859   months, the model assumes that this holds for each calendar month, and the final likelihood used in the
860   test is the product of the likelihoods of individual months.

861

862

863   GPS analysis

864   The high-resolution GPS time series at BARC in the center of the caldera (Fig. 3C) was obtained using RTKLIB
865   software, processing the receiver locations every 15 seconds as kinematic baselines from the HOFN
866   reference station in southeast Iceland. Other GPS data were analyzed using the GAMIT/GLOBK software,
867   version 10.6 using over 100 global reference stations to evaluate site positions in the ITRF08 reference
868   frame. For the regional network average daily station positions were estimated. For the caldera GPS station
869   (BARC) we furthermore divided the data into eight hour sessions using a 24 hour running window of
870   reference station and orbit data. In the processing we solve for station coordinates, satellite orbit and earth
871   rotation parameters, atmospheric zenith delay every two hours, and three atmospheric gradients per day.
872   The IGS08 azimuth and elevation dependent absolute phase center offsets were applied to all antennas and
873   ocean loading was corrected for using the FES2004 model.

874

875   InSAR analysis

876   We utilized X-band (wavelength 3.11 cm) radar images acquired by the COSMO-SkyMed constellation and
877   employed two-pass Interferometric Synthetic Aperture Radar (InSAR) analysis (75) to measure ground
878   deformation at Bárdarbunga caldera over 24-hr periods during which large caldera earthquakes occurred.
879   The interferograms were processed using DORIS software (76) and a merged LiDAR, intermediate TanDEM-
880   X, ASTER and EMISAR DEM was used to remove topographic fringes (77). To account for the large changes
881   in topography over the caldera during the eruption, we interpolated the digital elevation model, using data
882   from the continuous GPS station located inside the caldera. The wrapped interferometric phase values
883   were filtered using an adaptive filter (78) and unwrapped with SNAPHU software (79). The one-day
884   interferogram spanning September 17-18, 2014 was used to infer the location of faults that slipped during
885   this period, which included a large caldera (M5.3) earthquake (Fig. S7). We modelled the fault system as a
886   series of 30 rectangular vertical faults (79) with varying strike, and estimated location, size, minimum depth
887   beneath the surface, and slip for each segment. Note, the data could be fitted equally well with steeply
888   dipping faults, in either direction, but we fixed them to be vertical for convenience. The southern margin
889   did not slip in this 24-hour interval and the model therefore does not constrain the actual location of the
890   southern caldera fault. The contracting body at the base of the fault system was also modelled as a closing
891   rectangular dislocation with uniform contraction (79). We used a Markov-chain Monte Carlo approach to
892   estimate the multivariate probability distribution for all model parameters (80).

893

Petrological analysis and thermobarometry

895 Major element compositions of minerals and glasses were analyzed using a JEOL JXA-8230 electron
896 microprobe at the Institute of Earth Sciences, University of Iceland. Fluid inclusions within phenocrysts
897 were analysed by optical microscopy and confocal Raman spectroscopy (Horiba Jobin Yvon LabRAM HR800)
898 at the Bayerisches Geoinstitut, Bayreuth, Germany. Eruption temperatures calculated with different
899 thermometers (*81-83*) for the erupted lava are consistently in the range 1165-1180°C, in good agreement
900 with on-site measurements by thermal imaging cameras. Three independent thermobarometers were used
901 to constrain the depth of magma accumulation before the onset of the eruption; *(i) Glass thermobarometry*
902 was carried out using the fractional crystallization model of Yang et al. (*82*), which was calibrated using
903 basaltic melt compositions, *(ii) Clinopyroxene-Liquid Thermobarometry* was carried out based on the
904 clinopyroxene-liquid barometers published by Putirka (*84*) that rely on the pressure and temperature
905 dependence of Fe, Mg, Al and Na partitioning between pyroxenes and coexisting melt, and *(iii) CO_2 Density*
906 *Barometry* which is based on the principle that distance between the two Raman bands of CO_2 (in the
907 wavenumber region between 1250 and 1450 cm^{-1}) is a function of fluid density (*85*). In combination with
908 information on the temperature of the system, the entrapment pressure can be estimated based on the
909 equation of state of CO_2.

910

911 Subaerial gas composition analysis

912 The composition of the subaerial eruptive gases was measured by open-path Fourier Transform Infrared
913 spectrometer (FTIR) (*86*) on September 3, 19, 20 and 21 using the erupting lava as an infrared radiation
914 source, and Multi-Component Gas Analyzer System (MultiGAS) (*87*) on September 1, 21, October 8, January
915 26 and Feburary 6. The MultiGAS measurements were taken downwind from vent when the plume was
916 grounded. Major element composition and wt% of volatiles of the melt were defined using the average of
917 four clinopyroxene-hosted melt inclusions (*88*, *89*) and used as input to the D-COMPRESS magma/volatile
918 partition software (*90*). The model was run from atmospheric pressure to 600 MPa (18 km). The simulation
919 results indicate that the sulfur reaches 1600 ppm, the highest concentrations measured in melt inclusions
920 most representative of the pre-eruptive magma composition (*88*), at 470±100 MPa (14±3 km). This
921 estimate is partly dependent on the solubility constants provided for basalt. However, it convincingly
922 supports the petrological and geodetic estimates.

923

924 DEM modelling

925 We evaluated the role of pre-existing ring fault structures on the 2014-15 collapse by using the two-
926 dimensional Distinct Element Method (DEM) software PFC 5.0 (*90*). The DEM models comprise a 40 × 25 km
927 gravitationally-loaded assemblage of rigid circular particles that interact according to frictional-elastic
928 contact laws (*91*). Particles have a uniform size distribution, with radii between 60 m and 100 m, and a
929 density of 2700 kgm^{-3}. The model's basal and the lateral boundaries are frictionless rigid walls. Inter-particle
930 and particle-wall contacts have a Young's modulus of 70 GPa and a normal to shear stiffness ratio of 2.5.
931 The model comprises three regions (Fig. 5D): (i) A laccolith-like 'magma reservoir'. (ii) A fault-bound
932 reservoir 'roof'. (iii) The 'host rock' around the reservoir and roof. Within the reservoir, the contact friction
933 is 0.01 and particles are not bonded. Outside the reservoir, the contact friction coefficient is 0.5 and
934 particles are bonded with linear elastic beams. Bond tensile and shear strengths are 35 MPa in the roof and
935 70 MPa in the surrounding host rock. Note that fracturing of the weaker 'roof' zone will reduce the

936 assembly-scale strength and modulus here, locally by up to an order of magnitude (*27*), as suggested for
937 Bardabunga by Riel et al. (*32*). Pre-existing faults, extending from the lateral edges of the reservoir to a few
938 kilometres below the surface (Fig. 5D), are modelled by using a contact law for 'smooth' discontinuities in
939 poly-disperse particle assemblages (*92*). The normal and shear stiffness of these 'fault' contacts is 60
940 GPa/m. Withdrawal of magma is assumed to occur laterally out of the 2D model plane (Fig. 5D) and is
941 simulated by slowly reducing the areas of the reservoir particles. Displacements of surface particles were
942 smoothed by a standard moving mean method to minimize localized particle effects. Our modelling
943 comprised a series of forward simulations in which the dip of each fault was varied between 80-90 degrees,
944 initial fault depths varied from 1-3 km, and chamber width varied from 7.0-8.5 km. Chamber depth was
945 fixed at 12 km, based on the geobarometry data, to reduce the parameter space. The lateral position of the
946 chamber was allowed to vary depending on the fault geometry, so that the faults lay within the clouds of
947 hypocentres and projected upward to within the caldera. Effects of Young's modulus, strength and fault
948 friction were also systematically tested. Further details on DEM modelling of caldera collapse are given in
949 Holohan et al. (*27*, *93*).

950

951 <u>Geodetic depth model</u>

952 To determine the approximate depth of the magma chamber, we modelled post-rifting InSAR and GPS data
953 (Fig. S3) using a point pressure source in an elastic halfspace (*94*). The depth range at 95% confidence is 8-
954 12 km.

955

956

957 <u>Coupled caldera subsidence and eruption model</u>

958 We assume piston failure occurs approximately at a constant stress threshold, causing the pressure at the
959 top of magma chamber to remain constant on average. Therefore, we ignore compressibility and assume
960 that the density of the magma remains constant. The driving overpressure is then given by

961

962 $$\Delta P = \frac{W - F}{A} + \rho g h - \rho g d \qquad \qquad (1),$$

963

964 where *W* is the weight of the piston, *F* is the resistive force (friction), *A* is the cross sectional area of the
965 magma chamber, ρ is the density of the magma, *g* is gravitational acceleration, h is the height of magma
966 above the chamber exit point and *d* is the depth of the chamber exit point relative to the eruption site (Ext.
967 Data 7). Conservation of mass implies

968

969 $$A \frac{dh}{dt} = -\pi r^2 v \qquad \qquad (2),$$

970

971 where *v* is the mean magma flow speed and r is conduit radius. Assuming that the time-averaged resistive
972 force due to friction, *F,* and *d* remain constant, differentiating (1) and substituting (2) gives

973

974 $$\frac{d\Delta P}{dt} = -\rho g \frac{\pi r^2}{A} v$$ (3).

975

976 Assuming pressure loss due to viscous drag from laminar flow in a cylindrical pipe (Hagen Poiseuille flow)
977 and dynamic pressure loss on exit

978

979 $$\Delta P = \frac{8\eta L}{r^2} v + \frac{\rho}{2} v^2$$ (4)

980

981 $$\Rightarrow v = -\frac{8\eta L}{\rho r^2} + \sqrt{\left(\frac{8\eta L}{\rho r^2}\right)^2 + 2\frac{\Delta P}{\rho}}$$ (5).

982

983 We assume a cylindrical pipe, as models of thermal erosion predict that the cross section of a magma flow
984 channel will evolve to be circular in shape, but note that for a non-circular cross section, the first term will
985 still be proportional to the velocity, but with a different constant.

986

987 Expanding (5) gives

988 $$\Rightarrow v = -\frac{8\eta L}{\rho r^2} + \frac{8\eta L}{\rho r^2} + \frac{r^2 \Delta P}{8\eta L} + O\left(\frac{r^2}{\eta L}\right)^2 = \frac{r^2 \Delta P}{8\eta L} + O\left(\frac{r^2}{\eta L}\right)^2$$ (6).

989

990 Substituting (6) into (3) gives

991

992 $$\frac{d\Delta P}{dt} = -\frac{\pi \rho g r^2}{A}\left[\frac{r^2 \Delta P}{8\eta L} + O\left(\frac{r^2}{\eta L}\right)^2\right]$$ (7).

993

994 When *L* >> *r²*, this reduces to

995

996 $$\frac{d\Delta P}{dt} = -\frac{\pi \rho g r^4}{8A\eta L}\Delta P$$ (8)

997 $$\Rightarrow \Delta P = \Delta P_0 e^{-\frac{\pi \rho g r^4}{8A\eta L}t}$$ (9)

998

999   and

1000 $$h - h_\infty = (h_0 - h_\infty)e^{-\frac{\pi\rho g r^4}{8A\eta L}t}$$ (10).

1001

1002   A similar relationship has been derived to explain gravity-driven eruptions at Stromboli (*95*). Assuming that
1003 $h_0 - h_\infty$ is equal to the subsidence measured at the BARC GPS station, a best fit solution is $h_0 - h_\infty$ = 67.5 m
1004   and $\frac{\pi\rho g r^4}{8A\eta L}$ = 1.5 × 10^{-7} (Fig. 3B). A similar fit is obtained for magma flow rate and caldera volume change in
1005   Fig. 6B. Substituting ρ = 2700 kgm^{-3} (ref. *64*), g = 9.8 ms^{-2}, L = 47 km and v=22 Pa s using the average glass
1006   compositions of the Holuhraun lava (*96*), gives ΔP_0 = 1.7 MPa and $\frac{r^4}{A}$ = 1.5 × 10^{-5} m^2. Constraining the
1007   eruption rate to be 250 m^3/s on 31 August, gives A= 32 km^2 and r = 4.7 m. This can be considered the
1008   effective radius of the flow path assuming circular cross sectional area. A similar relation would hold for
1009   other possible geometrical forms of the flow path cross sectional area. Theoretically, the eruption would
1010   approach equilibrium (ΔP=0 in (1)) asymptotically, but choking of the conduit due to cooling, slow-moving
1011   magma is expected before that.

1012
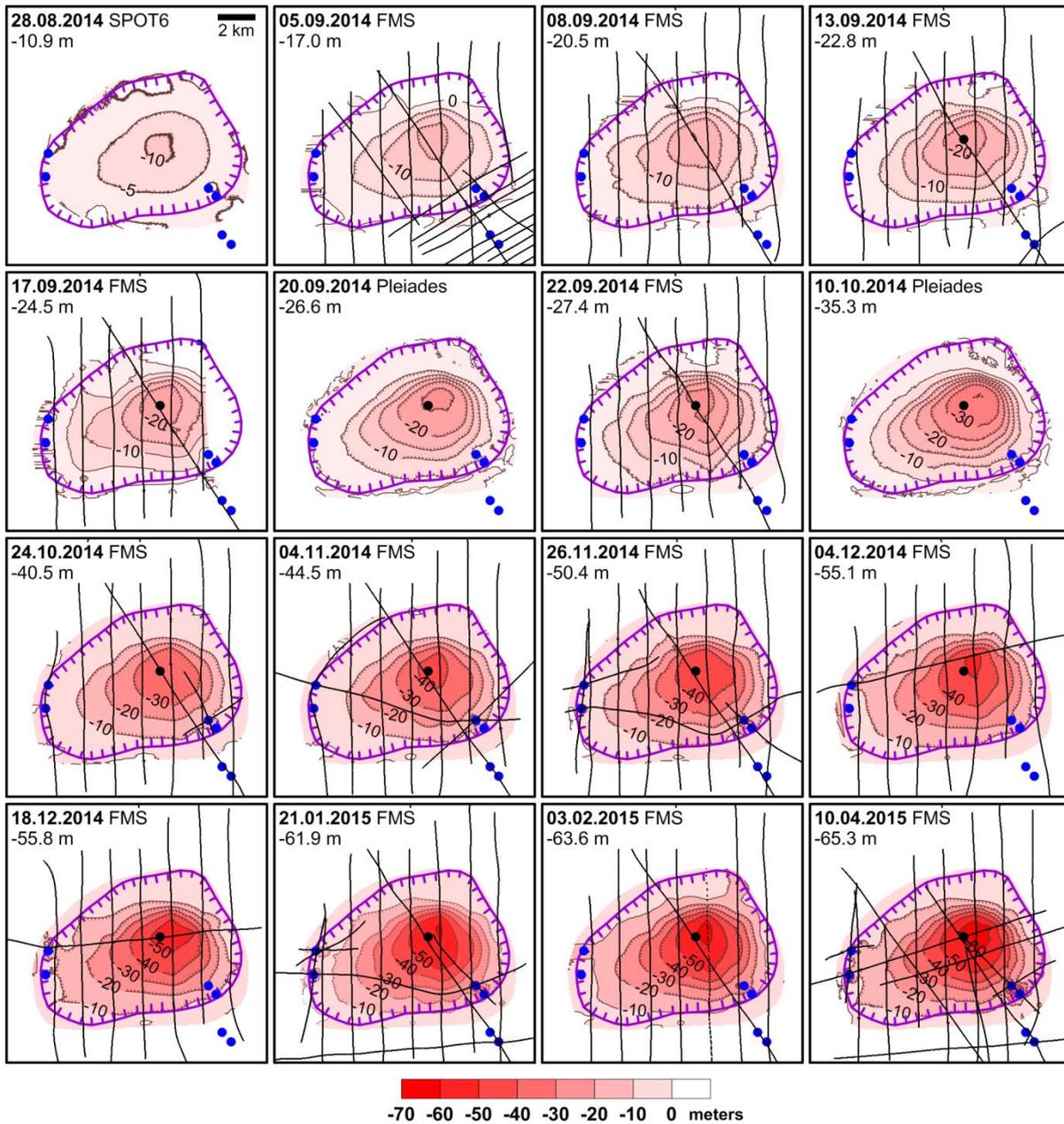
1013

Fig. S1.

Maps of collapse – margins as in Fig. 1C. The maps are corrected for ice flow (Fig. S2) and migration of reflector into the autumn 2014 surface due to propagation of cold wave into the firn in October-April (24). The number underneath the date gives the maximum subsidence. Three maps are obtained through satellite photogrammetry (28.08 – Spot 6, 20.09 and 10.10 from Pléiades) while the remaining 13 maps (marked as FMS) are obtained using an aircraft-combining radar altimetry and a submeter Differential GPS; the maps are made by interpolation between the profiles (shown as black lines)(24).

1021

41
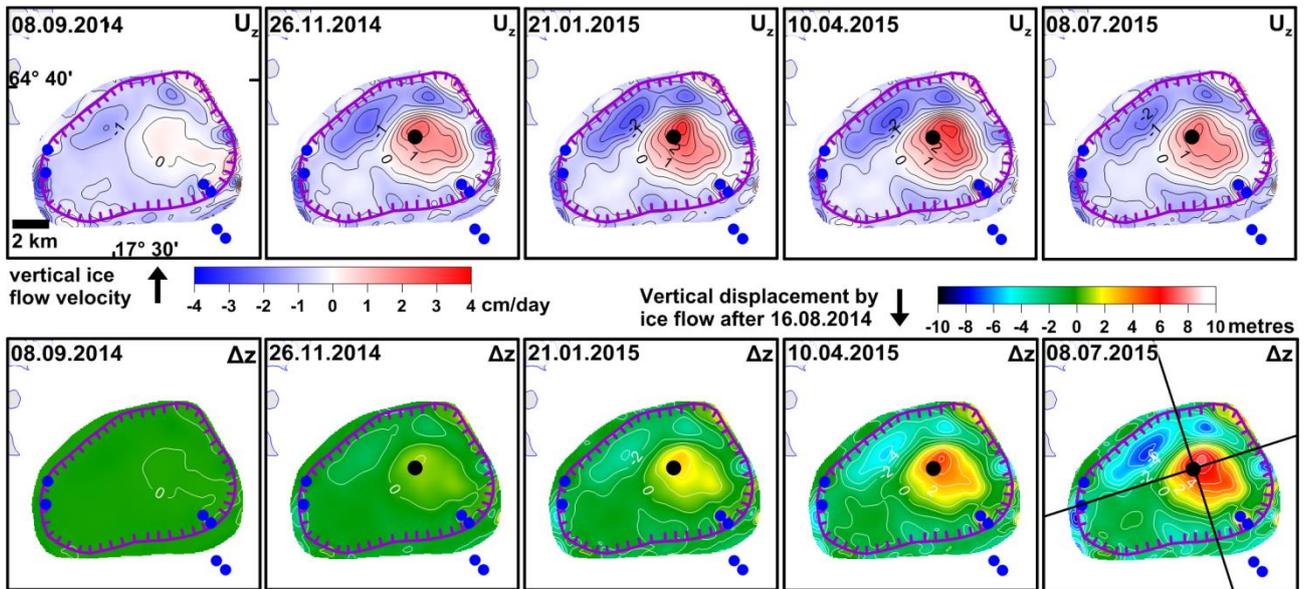
1022

Fig. S2

Results of 3-D Full-Stokes ice flow models (see Materials and Methods) of the response of the glacier
within the caldera to the subsidence for five dates spanning the period of collapse. The upper row shows
vertical ice flow velocity while the lower row shows the accumulated surface elevation change due to the
ice flow for the same dates. The model flow rates are constrained to fit the horizontal displacement of the
GPS station BARC in the caldera center from September to February (see Materials and Methods). The
maximum vertical ice flow velocity is modelled as having been about 3 cm per day on April 10, 2015. The
accumulated uplift for end of eruption on February 27 (Fig. 1C) is obtained by interpolation between
January 21 and April 10.

1033
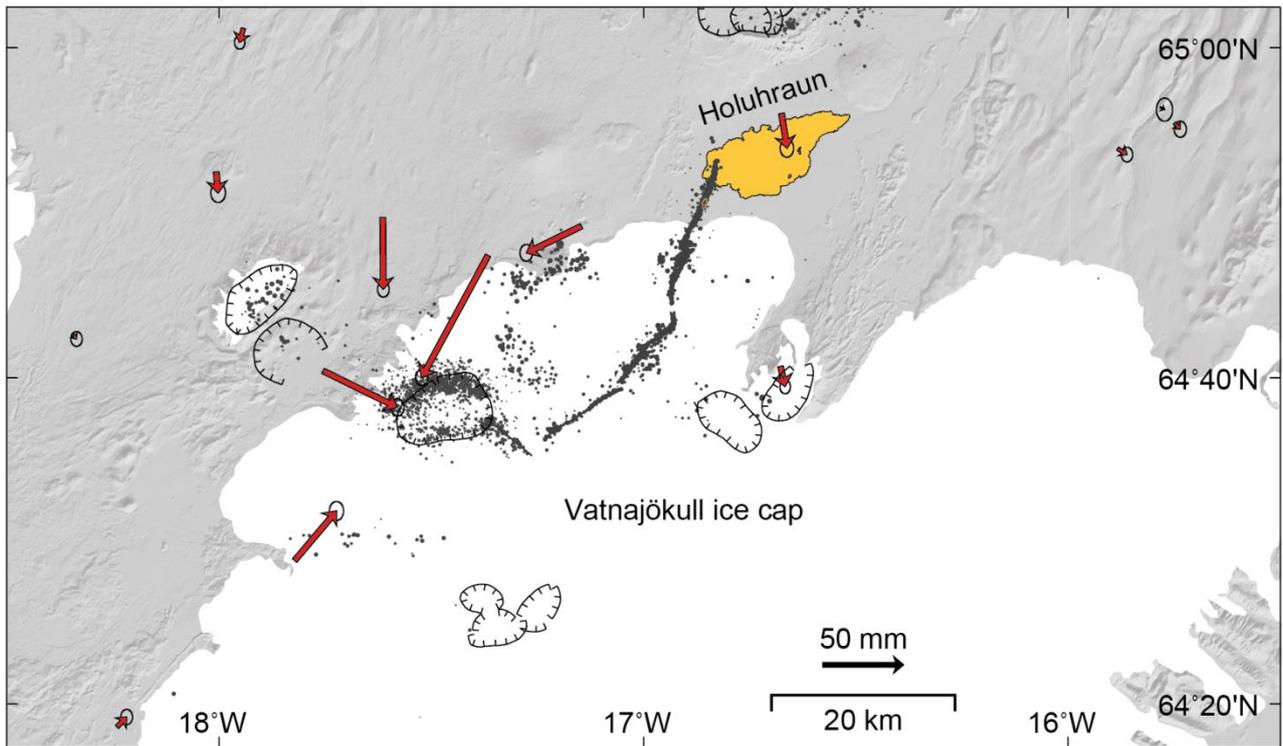
Fig. S3

GPS co-eruptive displacements, spanning September 21, 2014 until February 27, 2015, after the period of dyke opening had ended. The displacement field during the eruption shows consistent movements toward Bárdarbunga caldera suggesting deflation below the caldera. No other major deformation source can be observed during the eruption that can account for significant volume changes. Dots show relatively located earthquakes (20, 24).

1040
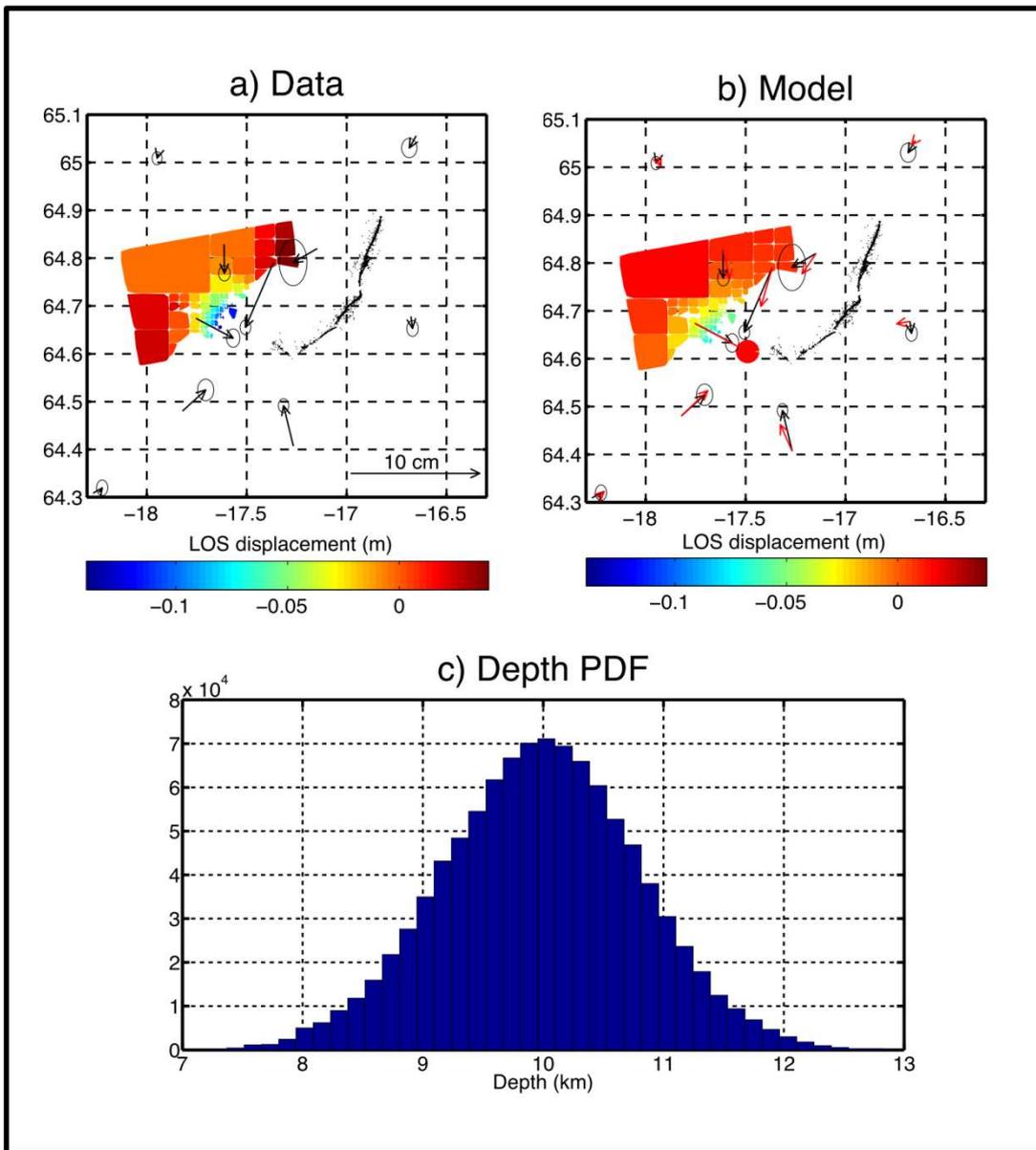
1041

**Fig. S4**

Geodetic model of regional deformation using a contracting point pressure source. The upper panel from left to right displays the input data (a) and model (b). GPS data in both panels and the CSK ascending interferogram in (a) span the period September 16 to November 7, 2014. The red circle in (b) shows the location of the point pressure source. The black dots represent the seismicity in the vicinity of the dike. The black lines are the inferred dike location. The lower figure (C) displays the probability distribution for depth of the point source from 1 million iterations, using a Markov chain Monte Carlo approach.

1049
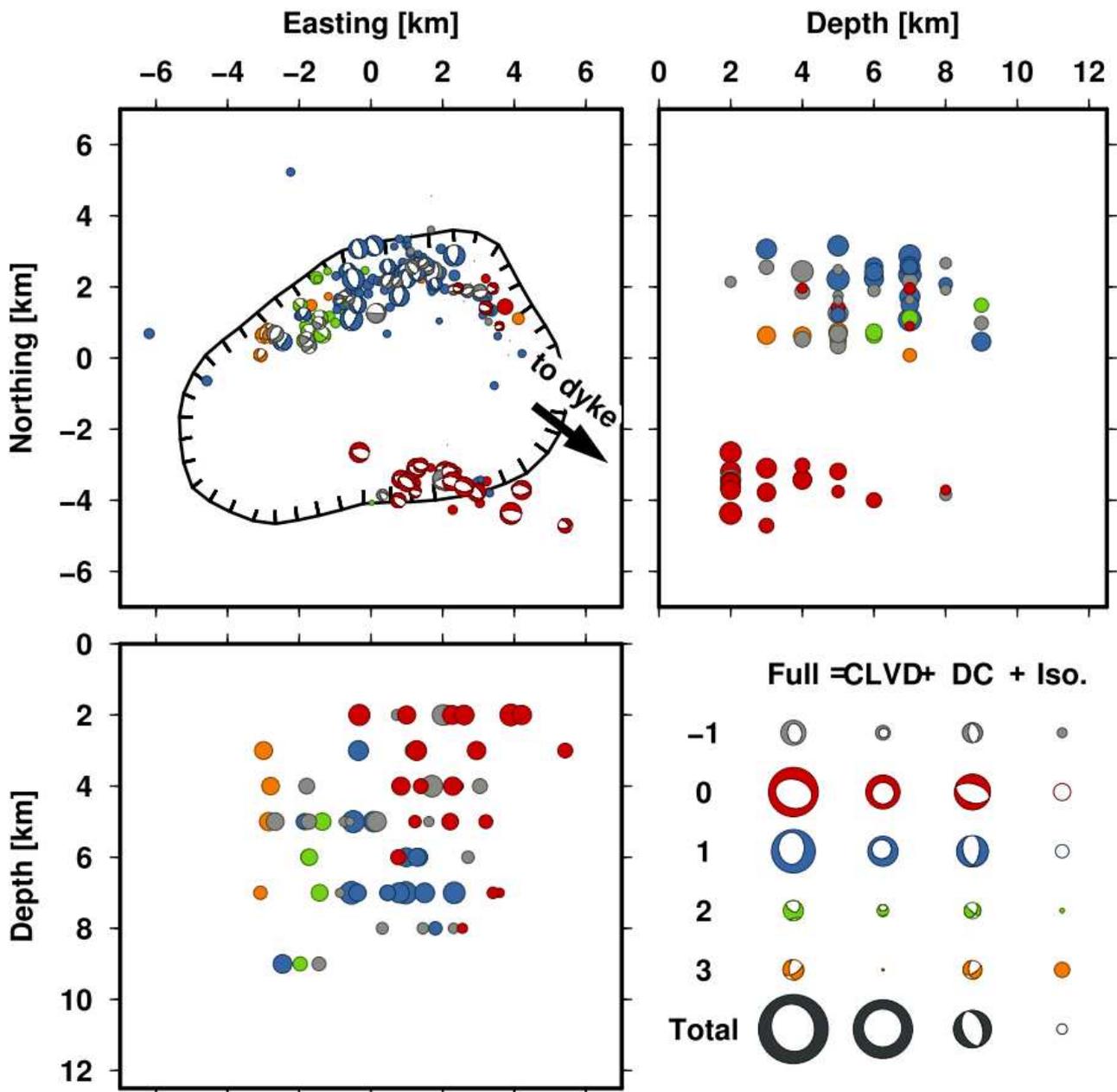
1050

Fig. S5

Source mechanisms of 77 M>5 events. Double couple (DC) components of the retrieved moment tensors (top left) and centroid locations for different cross sections (top right, bottom left). Focal mechanisms are colored according to the result of a DC clustering. The two main clusters are the red cluster, with a WNW-ESE normal faulting component, dominant at the southern rim; and the blue cluster, with N-S oriented normal faulting, characteristic of the northern rim. The standard decomposition is given in the bottom right panel for the four clusters, un-clustered (grey) and cumulative MTs (black).

1058
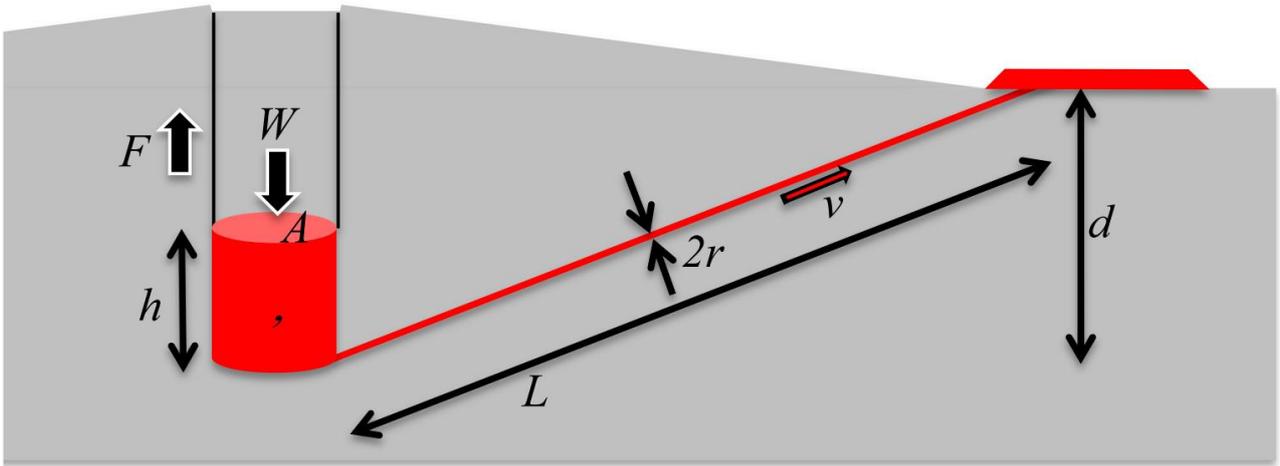
Fig. S6

Schematic of "piston collapse" model. Symbols as described in Materials and Methods

1062

1063

1064

1065

1066

1067

1068

1069

1070

1071
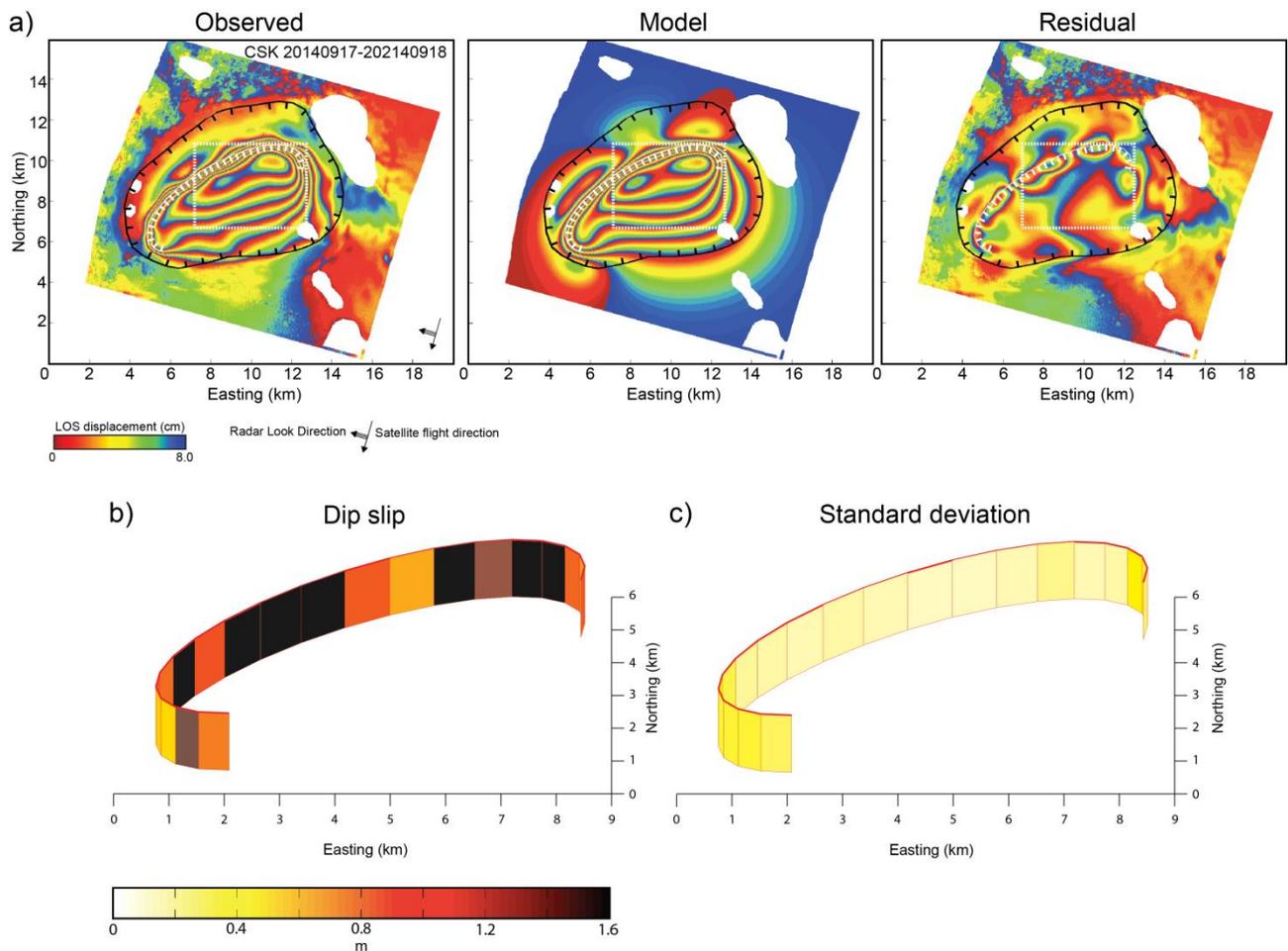
1072

1073

1074

1075

1076

1077

Fig. S7

Fault model for one-day interferogram. The data were acquired by COSMO-SkyMed constellation on 20140917 and 20140918. a) Comparison between observed, predicted and residual surface displacements. The black line outlines the outer caldera rim. The white lines mark the location of the inferred intra-caldera fault system (solid) and of the contracting body (dotted). As no slip is detected on the southern fault in the 24-hour period covered by the interferogram, the southern fault location is not constrained. Cauldrons, for which topography was not well constrained, are masked. b) Median of the posterior probability distribution of dip-slip on vertical fault segments, inferred from modelling. Color indicates the magnitude of slip. c) Standard deviation of the posterior probability distribution, using the same color scale as in b).
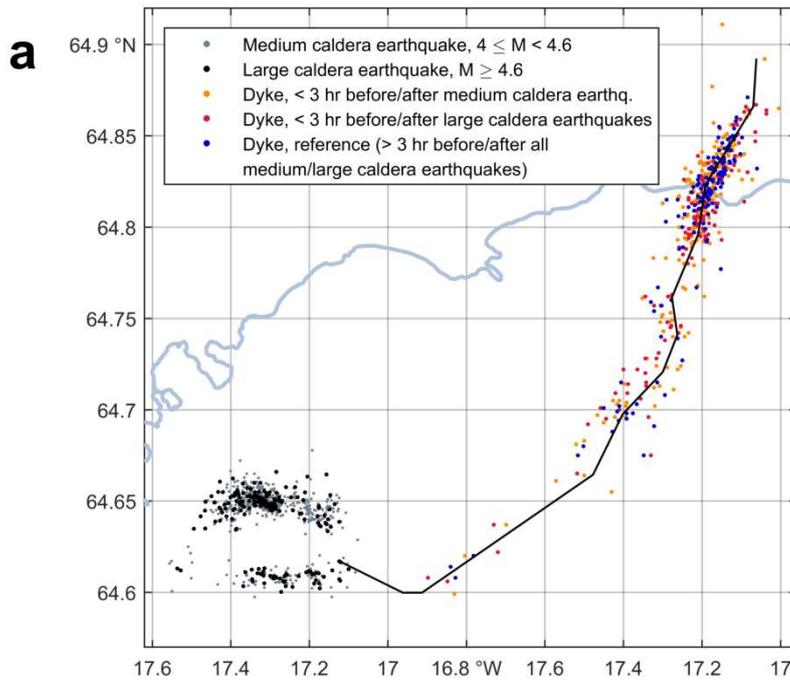
Fig. S8

Caldera-dike seismicity correlation. a) Geometry of correlated caldera-dike earthquakes. The dots show all dike earthquakes less than 2.5 km from the dike central line used for Figure 4a. b) Statistics of caldera-dyke earthquake correlations. Rate of dike earthquakes of magnitude $M \geq 0.8$ in time intervals shortly before and after large caldera earthquakes, of size ≥ 4.6, compared with the rate in reference intervals, consisting of all times during the respective period which are at least 3 hours before and at least 3 hours after all $M \geq$ 4.0 caldera earthquakes. c) An example of how data was chosen for the analysis (randomly chosen 3 days in October). Upper panel: caldera earthquakes M>4. Lower panel: dike earthquakes during the same period. Blue bins mark three hours before and after caldera earthquakes with M>4.5 used in the study. Yellow bins

1098 show data between significant (M>4) caldera earthquakes, used to estimate background seismicity in the

1099 dike. Pink shaded bins show data that were not used in the analysis (due to possible overlapping effects).
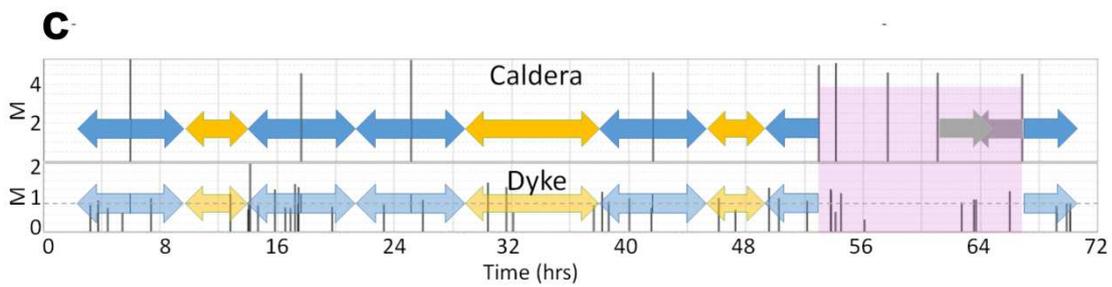
1100

1101

a

- Medium caldera earthquake, $4 \le M < 4.6$
- Large caldera earthquake, $M \ge 4.6$
- Dyke, < 3 hr before/after medium caldera earthq.
- Dyke, < 3 hr before/after large caldera earthquakes
- Dyke, reference (> 3 hr before/after all medium/large caldera earthquakes)

b

Period (2014)	Reference time, total days	Reference rate in dyke (earthq./hr.)	No. of $M \ge 4.6$ earthquakes in caldera	Intervals 0–3 hours before $M \ge 4.6$ caldera earthquakes			Intervals 0–3 hours after $M \ge 4.6$ caldera earthquakes		
				Total hours	No. of eq. in dyke	Rate (eq./hr.)	Total hours	No. of eq. in dyke	Rate (eq./hr.)
01–06 Sept.	3.1	7.04	8	19	132	6.85	19	140	7.26
07–12 Sept.	2.6	2.58	11	30	66	2.20	30	67	2.23
13–18 Sept.	3.1	1.39	9	21	30	1.40	21	27	1.26
19–24 Sept.	2.6	0.85	10	28	26	0.94	28	21	0.76
25–30 Sept.	1.3	0.47	10	29	23	0.81	29	20	0.70
Oct. 2014	5.0	0.14	74	179	44	0.25	179	47	0.26
Nov. 2014	4.2	0.14	25	64	19	0.30	64	12	0.19
Dec. 2014	11.0	0.09	15	42	5	0.12	42	3	0.07
Jan. 2015	14.8	0.19	13	39	10	0.26	39	9	0.23
1–21 Feb. 2015	18.6	0.10	3	9	1	0.11	9	3	0.33

c

Caldera

Dyke

Time (hrs)

1102

1103

1104

1105